

Marie Bøe Henriksen

# Hyperspectral Imager Calibration and Image Correction

Master's thesis in Cybernetics and Robotics

Supervisor: Tor Arne Johansen

June 2019





Norwegian University of  
Science and Technology

# Hyperspectral Imager Calibration and Image Correction

Master's thesis in Cybernetics and Robotics

Submission date: June 2019

Supervisor: Tor Arne Johansen

Co-supervisor: Fred Sigernes, Joseph Landon Garrett

Norwegian University of Science and Technology  
Department of Engineering Cybernetics



## Abstract

Algal blooms and other oceanographic phenomena will be detected by hyperspectral imagers from air- and spaceborne platforms, among others, as a part of the Hyperspectral Smallsat for Ocean Observation (HYPSO) mission. For the collected data to be usable, the hyperspectral instruments must be calibrated and characterised before use. The first goal of this project was therefore to set up calibration procedures for spectral and radiometric calibration of the Hyperspectral Imagers (HSIs), and further test these procedures by calibrating two imagers. The second goal was to detect spectral and spatial misregistrations in the system, also known as smile and keystone, and make corrections for these effects. Spectral and radiometric calibration procedures were set up, and two imagers, the HSI V4 and the HSI V6, were calibrated. After spectral calibration, the spectral range was calculated, and was found to be 299 to 1015 nm for the HSI V4, and 378 to 851 nm for the HSI V6. Further, a set-up to detect smile and keystone effects was designed and built, consisting of a collimator lens, a striped pattern, and spectral light sources. Algorithms were developed to detect the effects by using the resulting intersection points in the spectrogram. Corrections were then made by mapping the detected points to a reference grid. While correction of HSI V4 spectrograms showed clear improvement, the algorithms used to obtain the distortion model can be further improved to achieve even better performance. Other effects characterised include the spectral bandpass of the imagers, and the linearity of the sensor response. Spectral bandpass for the HSI V4 was estimated to be 2.66 nm, and 2.84 nm for the HSI V6. The sensor response of the HSI V4 was found to be linear.



## Sammendrag

Hyperspektrale kameraer, ombord blant annet droner og småsatellitter, skal detektere algeoppblomstring og andre havfenomener langs norskekysten. Dette er en del av prosjektet HYPSO, som står for "hyperspektral småsatellitt for havobservasjon". For at bildene skal være brukbare må kameraene være kalibrert og karakterisert før bruk. Det første målet i denne oppgaven var derfor å sette opp prosedyrer for spektral og radiometrisk kalibrering, og deretter kalibrere to hyperspektrale kameraer. Det andre målet var å detektere kjente feileffekter kalt "smile" og "keystone", samt korrigere for disse. Prosedyrer for spektral og radiometrisk kalibrering ble utviklet, og de hyperspektrale kameraene HSI V4 og HSI V6 ble kalibrert. Etter spektral kalibrering ble spektral rekkevidde regnet ut, og estimert til 299 til 1015 nm for HSI V4, og 378 til 851 nm for HSI V6. Videre ble et oppsett for å detektere "smile" og "keystone" utviklet, bestående av en kollimator, et stripete mønster og spektrale lyskilder. Effektene ble detektert ved å bruke skjæringspunktene dannet i spektrogrammet og videre korrigert for ved å transformere skjæringspunktene over på et referansegitter. Korreksjon av bilder fra HSI V4 viste en klar forbedring, men feilmodellen kan bedres. I tillegg ble spektral båndpass og lineæritet av sensorresponsen karakterisert. Spektral båndpass for HSI V4 ble estimert til 2.66 nm, og 2.84 nm for HSI V6. Resultatene viser at HSI V4 har tilnærmet lik lineær sensorrespons.



## Preface

The work in this thesis is a continuation of the work presented in the specialisation project "Hyperspectral Imager Calibration and Characterisation" [1], during the fall of 2018. The main parts of Chapter 1, parts of Chapter 2 (mainly Section 2.1, Section 2.2.1, Section 2.3, parts of Section 2.4, and Section 2.5.1), parts of Chapter 3 (mainly Section 3.1.1, parts of Section 3.2, and parts of Section 3.3), as well as Appendix B, are all based upon the work presented in the specialisation project.

For both the specialisation project and this thesis, hyperspectral imagers designed by Fred Sigernes were used, and an introduction to the concept of hyperspectral imaging was given by him in the course TTK20 Hyperspectral remote sensing, in the fall of 2018. The collimator set-up used for smile and keystone correction was also mainly designed by Fred. The calibration equipment for spectral and radiometric calibration was available from mid-September, and Elizabeth Prentice was of great help when collecting data the first months. Code for reading the images was developed by Joe Garrett, which also helped with the code for spectral calibration.

As a part of this thesis, the procedures for data collection were made, the physical collimator set-up was built and tested, and data for calibration and characterisation was acquired. Further, code was written to calculate and apply the calibration and correction coefficients, and for various analysis of the data. A side project not included in this thesis was radiation testing of the sensor and lenses used in the HSI V6, where a characterisation set-up was designed and built to detect changes in the radiometric response due to radiation, and code written for analysis of the data gathered.

The work in this thesis is also summarised in the paper "Real-time Corrections For A Low-cost Hyperspectral Instrument" submitted to the Workshop on Hyperspectral Image and Signal Processing: Evolution in Remote Sensing (WHISPERS) 2019, with focus on how the calibration and correction coefficients from this thesis can be applied real-time for autonomous operations.



### **Acknowledgement**

I would like to thank Fred Sigernes for sharing his knowledge on hyperspectral imaging, and for his help on designing the set-up used to detect smile and keystone in the imagers. Further, I would like to thank Joe Garrett for all his help with analysing the calibration data, and Elizabeth Prentice for collaboration on the calibration procedures and data collection. I would also like to thank Lise Lyngsnes Randeberg for letting us use the optical calibration lab, including the integrating sphere and the calibration lamps, at NTNU. Finally, a special thanks should be given to Tor Arne for advising and supporting me throughout the semester.



# Table of Contents

|  |          |
|--|----------|
| Abstract                                     | i        |
| Sammendrag                                   | iii      |
| Preface                                      | v        |
| Acknowledgements                             | vii      |
| Table of Contents                            | ix       |
| List of Abbreviations                        | xi       |
| <b>1 Introduction</b>                        | <b>1</b> |
| <b>2 Background Theory</b>                   | <b>5</b> |
| 2.1 Imaging Optics . . . . .                 | 5        |
| 2.1.1 Definitions . . . . .                  | 6        |
| 2.1.2 Imaging System . . . . .               | 8        |
| 2.2 Hyperspectral Imaging . . . . .          | 13       |
| 2.2.1 Remote Sensing Techniques . . . . .    | 13       |
| 2.2.2 Hyperspectral Data . . . . .           | 15       |
| 2.3 Calibration . . . . .                    | 16       |
| 2.3.1 Spectral Calibration . . . . .         | 16       |
| 2.3.2 Radiometric Calibration . . . . .      | 17       |
| 2.4 Smile and Keystone . . . . .             | 19       |
| 2.4.1 Detection . . . . .                    | 21       |
| 2.4.2 Correction . . . . .                   | 23       |
| 2.4.3 Requirements . . . . .                 | 24       |
| 2.5 Other Effects . . . . .                  | 25       |
| 2.5.1 Spectral Bandpass . . . . .            | 25       |
| 2.5.2 Linearity of Sensor Response . . . . . | 26       |
| 2.5.3 Signal-to-Noise Ratio . . . . .        | 26       |

|          |   |           |
|----------|---|-----------|
| 2.5.4    | Polarisation Sensitivity . . . . .      | 27        |
| 2.5.5    | Stray Light . . . . .                   | 28        |
| 2.5.6    | Temperature Dependence . . . . .        | 29        |
| <b>3</b> | <b>Methods</b>                          | <b>31</b> |
| 3.1      | Equipment . . . . .                     | 31        |
| 3.1.1    | HSI V4 and HSI V6 . . . . .             | 32        |
| 3.1.2    | Collimator Set-up . . . . .             | 33        |
| 3.2      | Spectral Calibration . . . . .          | 34        |
| 3.3      | Radiometric Calibration . . . . .       | 35        |
| 3.4      | Characterisation . . . . .              | 37        |
| 3.4.1    | Smile and Keystone . . . . .            | 37        |
| 3.4.2    | Spectral Bandpass . . . . .             | 39        |
| 3.4.3    | Sensor Response . . . . .               | 40        |
| <b>4</b> | <b>Results and Discussion</b>           | <b>41</b> |
| 4.1      | Spectral Calibration . . . . .          | 42        |
| 4.2      | Radiometric Calibration . . . . .       | 43        |
| 4.2.1    | Dark Current . . . . .                  | 43        |
| 4.2.2    | Radiometric . . . . .                   | 45        |
| 4.3      | Characterisation . . . . .              | 47        |
| 4.3.1    | Smile and Keystone . . . . .            | 47        |
| 4.3.2    | Spectral Bandpass . . . . .             | 49        |
| 4.3.3    | Sensor Response . . . . .               | 51        |
| <b>5</b> | <b>Conclusion and Further Work</b>      | <b>53</b> |
|          | <b>References</b>                       | <b>55</b> |
|          | <b>Appendices</b>                       | <b>59</b> |
| <b>A</b> | <b>Data Collection Procedures</b>       | <b>61</b> |
| A.1      | Spectral Calibration . . . . .          | 61        |
| A.2      | Radiometric Calibration . . . . .       | 62        |
| A.2.1    | Dark Current Data . . . . .             | 62        |
| A.2.2    | Radiometric Data . . . . .              | 62        |
| A.3      | Smile and Keystone Correction . . . . . | 64        |
| <b>B</b> | <b>Lamp Certificate, ISS-30-VA</b>      | <b>65</b> |

# List of Abbreviations

|         |   |
|---------|---|
| AMOS    | Center for Autonomous Marine Operations and Systems |
| AOI     | Area Of Interest                                    |
| ASV     | Autonomous Surface Vehicle                          |
| AUV     | Autonomous Underwater Vehicle                       |
| CCD     | Charge-Coupled Device                               |
| CHB     | Calibration Home Base                               |
| CMOS    | Complementary Metaloxide Semiconductor              |
| CubeSat | U-Class Spacecraft                                  |
| DLR     | German Aerospace Center                             |
| DN      | Digital Number                                      |
| DTU     | Technical University of Denmark                     |
| EnMAP   | Environmental Mapping and Analysis Program          |
| EO      | Earth Observation                                   |
| FFI     | Norwegian Defence Research Establishment            |
| FOV     | Field Of View                                       |
| FPA     | Focal Plane Array                                   |
| FWHM    | Full Width at Half Maximum                          |
| GCP     | Geometric Control Point                             |
| GSF     | Glare Spread Function                               |
| HICO    | Hyperspectral Imager for the Coastal Ocean          |
| HSI     | Hyperspectral Imager                                |
| HYPSONO | Hyperspectral Smallsat for Ocean Observation        |
| HypIRI  | Hyperspectral Infrared Imager                       |
| IDS     | Imaging Development Systems                         |
| LSF     | Line Spread Function                                |
| NCC     | Normalised Cross Correlation                        |
| NIST    | National Institute of Standards and Technology      |

|          |  |
|----------|--|
| NTNU     | Norwegian University of Science and Technology |
| PC       | Phase Correlation                              |
| PSF      | Point Spread Function                          |
| SDF      | Stray Light Distribution Function              |
| SmallSat | Small Satellite                                |
| SNR      | Signal-to-Noise Ratio                          |
| SLFS     | Spectral Line Spread Function                  |
| UAV      | Unmanned Aerial Vehicle                        |
| UNIS     | University Centre in Svalbard                  |
| VNIR     | Visible and Near-Infrared                      |

# 1 | Introduction

Hyperspectral imaging, also known as imaging spectroscopy, is an imaging technique used to combine two dimensional spatial data with a third dimension of spectral data. Spectral information from hundreds of narrow bands are obtained by recording radiance in, and near, the visible spectrum. The data collected is therefore often called a "hyperspectral data cube". A similar instrument is the multispectral imager, which is based on the same technology, but records information from fewer, and often wider, spectral bands. In this report, two Hyperspectral Imagers (HSIs) are calibrated and characterised to ensure better quality of the data obtained. A more detailed explanation of the hyperspectral imager and how it works is given in Section 2.2.

In the early development of hyperspectral imaging systems, the instruments were mainly oriented towards remote sensing applications [2]. Data acquired from these types of operations can be used within disciplines such as oceanography, precision farming, forestry and geology, among others [3]. For oceanographic purposes, detection and classification of algae is one possible application. Algal blooms can produce vividly coloured displays from the algae cells accumulating on the water surface. The blooms can be friendly, but some may also be harmful due to their production of internal toxins, their sheer biomass, or their physical shape. The toxins produced may kill fish and shellfish, and also harm human consumers. Death of birds and mammals related to harmful algal blooms and their toxins have also been recorded, giving huge public and economic concerns when they occur. High biomass accumulation of algae can lead to environmental damage, including hypoxia, anoxia, and shading of submerged vegetation. This may further lead to a multitude of negative environmental consequences. [4] Algal blooms have been recorded along the Norwegian coast since 1985. Some events, such as toxic blooms in the Ofoten-Tysfjord area in 1991 [5], in Boknafjord in 1989, 1990 and 1993, and outside of Bergen in 1993, have caused tonnes of atlantic salmon and rainbow trout to be killed [6]. Even though less than 2% of some 5000 species of marine microalgae described worldwide are known to be harmful or toxic, the percentage appears to be increasing [7].

Events such as algal blooms can easily be detected using optical instruments, due to the blooms' clear surface signatures in the spectral domain. An algal bloom may develop in only a few days, and disappear equally quickly. Automatic detection and measurements are

therefore required to adequately describe the dynamics of the blooms. The algal blooms can be detected by measuring the changes in the absorption properties of the ocean, and may further be classified using models to provide information on whether the bloom is likely to be harmful or not. [6] The information acquired using a hyperspectral imager from airborne platforms can therefore be used to detect algal blooms as they appear, identify them and characterise their spatial extent, as well as observe other phenomena happening in the Visible and Near-Infrared (VNIR) spectrum [8]. This is the background motivation for the Hyperspectral Smallsat for Ocean Observation (HYPSO) mission [9], which is a satellite mission initiated by the Norwegian University of Science and Technology (NTNU) Small Satellite (SmallSat) Lab. The SmallSat Lab focuses on designing, building and operating small satellites for observing the Norwegian coastline and ocean. As described in [8], the HYPSO satellite will observe the ocean along the Norwegian coast, specifically targeted to detect algal blooms, phytoplankton, river plumes, and so on.

The use of hyperspectral sensors in a spaceborne mission is no new idea, however. Other Earth Observation (EO) missions such as EO-1, with the instrument Hyperion [10], and the Hyperspectral Imager for the Coastal Ocean (HICO) mission [11], among others, have previously used HSIs for collecting data. There are also other missions planned for the near future, such as Environmental Mapping and Analysis Program (EnMAP), and Hyperspectral Infrared Imager (HypIRI), as mentioned in [12]. These satellites are all larger satellites, which makes them a lot more expensive. The HYPSO satellite, on the other hand, is a U-Class Spacecraft (CubeSat), which is much smaller and costs less both to produce and to launch. This gives an opportunity to produce more satellites and make them work together to increase temporal coverage and redundancy. To increase the Signal-to-Noise Ratio (SNR), which is crucial for ocean colour observation, a slew manoeuvre will be performed to obtain several overlapping images of the targeted area [8].

The HYPSO mission is a project under the Center for Autonomous Marine Operations and Systems (AMOS). After launch, the satellite will work together with Autonomous Underwater Vehicles (AUVs), Autonomous Surface Vehicles (ASVs) and Unmanned Aerial Vehicles (UAVs). They will execute coordinated missions to obtain a greater amount of information from the area of interest, creating an autonomous multi-agent system for marine observations. [8] Hyperspectral data from the satellite can, for example, be used to detect a potential harmful algal bloom. UAVs, also equipped with an HSI, can be sent off to investigate the algal bloom further, giving a better resolution view of a smaller part of the targeted area. ASVs can be used to collect in-situ measurements, such as water samples

to investigate the algae further in the lab, and AUVs can be deployed to collect information from underneath the water surface, since the air- and spaceborne instruments only collect information from the upper layers of the ocean.

Space- and airborne instruments require proper characterisation before use, as possibilities for performing characterisation procedures after launch are very limited. If the instrument is not calibrated and characterised well enough, the data provided by the sensor will in worst case be deemed unusable for the planned applications. [3] Characterisation refers in this report to the act of describing distinctive characteristics of the imager, while calibration is the act of setting parameters of the imager by comparing the performance with known standards. For a hyperspectral imager, spectral and radiometric calibration are needed to provide necessary information about the recorded data. Spectral calibration gives the relationship between the pixel number and corresponding wavelength value, while the radiometric calibration provides the relationship between sensor count and true radiance. The calibrations are further described in Section 2.3. Characterisation of the instrument is also needed to make corrections for effects corrupting the data, and to determine uncertainties inherent in the measurements. Some unwanted effects may arise due to spectral and spatial misregistrations, commonly referred to as smile and keystone, respectively. Characterisation, and correction, of these effects are one of the main goals of this project. Smile and keystone are further described in Section 2.4. Other features characterised in this report includes the spectral bandpass of the system, and the linearity of the sensor response. In addition, the dynamic range, the temperature dependency, stray light, and polarisation sensitivity should also be characterised, as mentioned in [13]. Characterisation of these effects, however, is a part of the future work of this project.

There are several places in the world that have the equipment and knowledge needed on how to calibrate and characterise a hyperspectral imager. Some examples are the Calibration Home Base (CHB) at the German Aerospace Center (DLR) in Germany [14], and the optical lab at the Norwegian Defence Research Establishment (FFI) in Norway. There is also a lab for radiometric calibration at the University Centre in Svalbard (UNIS). Sending the imager to different locations costs time and money, and there is no guarantee that the imager is still fully calibrated after transportation back from the calibration lab. Vibrations and other external factors may affect the imager, which can result in minor physical changes in the system and give the need for a new calibration. That the calibration may be invalid after transportation is also the reason why the imager must be re-calibrated after launch when being used for remote sensing [15].

A radiometric sphere and four spectral lamps, further described in Section 3.1, are available for radiometric and spectral calibration at NTNU. Time is a critical factor in the HYPSONO mission, as NTNU SmallSat Lab intends to have a continuous pipeline of spacecraft in an ongoing process of development, test and operations [9]. The ability to calibrate the hyperspectral imager at NTNU is therefore highly beneficial for NTNU SmallSat Lab in terms of the HYPSONO mission and other hyperspectral missions.

The aim of this project is therefore to set up spectral and radiometric calibration procedures and perform these on hyperspectral imagers using the existing equipment at NTNU, and further investigate and implement a method for detecting and correcting smile and keystone effects in these imagers.

The remainder of this report is divided into four chapters. Chapter 2 gives some background theory regarding hyperspectral imaging, and calibration and characterisation of such imagers. In Chapter 3 the equipment used is described, as well as the calibration and characterisation set-ups and procedures used in this project. The results are presented and discussed in Chapter 4, and Chapter 5 holds the conclusion and outlines further work that describes what can be done to improve the calibration procedures and expand the characterisation process in the future.

## 2 | Background Theory

To understand the need for, and the importance of, hyperspectral imager calibration and characterisation, a basic understanding of imaging systems in general is needed. Knowledge on the hyperspectral imagery concept itself is also essential. This section therefore gives a short introduction to the basic concepts needed for understanding these systems.

Theory on imaging systems in general is presented in Section 2.1, with focus on the components used in hyperspectral imaging, such as the grating and the optical diagram of a spectrograph. Section 2.2 explains the hyperspectral imagery concept, and describes the pushbroom technique, which is the imaging technique used for the HSIs in this project. Background on spectral and radiometric calibration is given in Section 2.3, together with a brief summary on how these calibrations may be performed, and what equipment is required. An introduction to spectral and spatial misregistrations, namely smile and keystone, as well as previous work done on how to detect and make corrections for these effects is presented in Section 2.4. Other effects that may be characterised, including spectral bandpass, linearity of the sensor response, polarisation sensitivity and stray light, are finally presented in Section 2.5.

### 2.1 Imaging Optics

Imaging systems consist of several optical components, and different systems are used for different purposes. A basic understanding of the behaviour of light through these systems is beneficial for understanding the greater concepts of why imperfections in the design or construction may cause different unwanted effects in the final product. The importance of these effects, and mitigation options, depends on the understanding of their cause, which makes it important to introduce some theory on basic imaging optics.

This section starts by introducing some relevant terminology and units used when observing light. Further, theory for understanding the imaging systems in general is presented, and elements typically used in hyperspectral designs are introduced. The theory presented is based on [2], [16] and [17].

### 2.1.1 Definitions

First, some terminology, as well as some important units used later both within this section and further throughout the report, will be introduced.

#### Solid Angle

The solid angle,  $\Omega$ , is defined as

$$\Omega = \frac{A}{r^2}, \quad (2.1)$$

where  $A$  is the area of a sphere segment, and  $r$  the radius of the sphere. The solid angle is measured in steradians, or square radians,  $[sr]$ . An illustration can be seen in Figure 2.1.

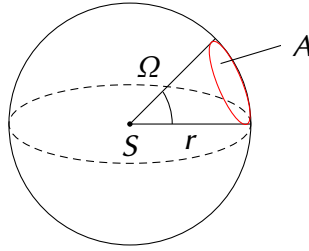


Figure 2.1: Definition of solid angle,  $\Omega$ , where  $S$  is the source point,  $r$  the radius of the sphere, and  $A$  the area of a sphere segment.

#### Flux, Intensity and Radiance

The *radiant flux*,  $\Phi_e$ , in the system is defined as the number of radiant energy emitted from a source,  $S$ , per unit time into a solid angle,  $\Omega$ , so that

$$[\Phi_e] = W. \quad (2.2)$$

*Intensity*,  $I$ , is further defined as the radiant flux per unit solid angle,

$$[I] = \frac{W}{sr}. \quad (2.3)$$

*Radiance*,  $L$ , is then defined as the intensity through a unit surface area, or radiant flux per unit projected area and solid angle,

$$[L] = \frac{W}{m^2 sr}, \quad (2.4)$$

and *irradiance*,  $E$ , is defined as the power incident on or passing through a unit surface area,

$$[E] = \frac{W}{m^2}. \quad (2.5)$$

Further, *spectral radiance*,  $L_\lambda$ , and *spectral irradiance*,  $E_\lambda$ , are defined as radiance per wavelength and irradiance per wavelength, respectively,

$$[L_\lambda] = \frac{W}{m^2 \text{ nm sr}} \quad \text{and} \quad [E_\lambda] = \frac{W}{m^2 \text{ nm}}. \quad (2.6)$$

### Reflectance, Transmittance and Absorptance

The term *reflectance* describes the fraction of light that is reflected from a surface. A *reflectance spectrum* is a plot of reflectance as a function of wavelength. *Transmittance* describes the fraction of light that passes through a substance. The transmittance of an object can be described by its *transmission coefficient*. Further, *absorptance* is a measure of the rate of decrease in the light intensity as it passes through a substance. This should not be confused with *absorbance*, which refers to the physical process of absorbing light.

### Interference and Diffraction

*Interference* is the result of individual wave sources interacting with each other, while *diffraction* is caused by a wave distorted by an obstacle. An illustration of interference and diffraction can be seen in Figure 2.2.

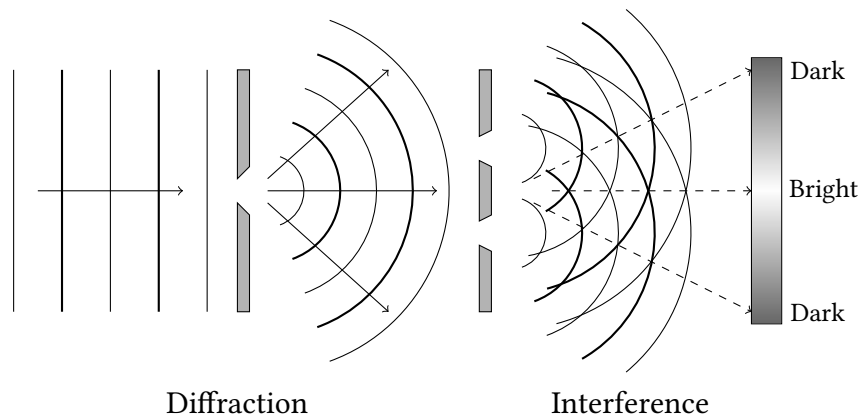


Figure 2.2: Illustration of diffraction as the light is distorted by an obstacle, and interference as two wave sources interact with each other resulting in an interference pattern.

### 2.1.2 Imaging System

In an imaging system, the *optical axis* is the straight line that passes through the centres of curvature of the lenses in the system, as seen in Figure 2.3.

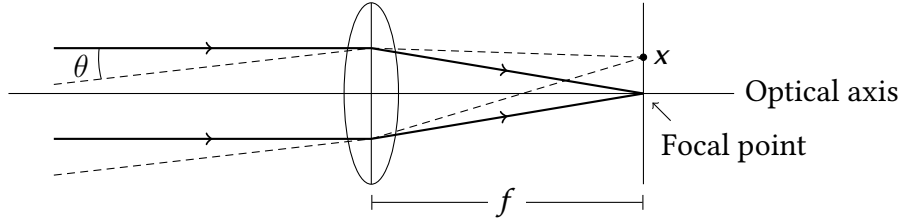


Figure 2.3: Illustration of the optical axis, and the focal length  $f$ .  $\theta$  denotes the angle of the incident wave, and  $x$  the shift in the image plane. Based on illustration found in [17].

Rays that are close or parallel to the optical axis, also known as *paraxial rays*, converge at a point on the axis called the *focal point*. Extending this point into a plane perpendicular to the optical axis gives the *focal plane*, which is where the image is focused. The scale of the image is further defined by the *focal length*,  $f$ , which is the distance between the centre of the front lens and the focal point. If  $x$  is the shift in image point in the focal plane for a tilt,  $\theta$ , in the incident wave on the lens, the focal length is given by

$$f = \frac{x}{\tan \theta}. \quad (2.7)$$

The *f-number*,  $F/\#$ , is further defined as

$$F/\# = \frac{f}{D}, \quad (2.8)$$

where  $f$  is the focal length and  $D$  is the aperture of the system. A higher f-number gives a smaller opening for the light to pass through. Light from a smaller area will then reach the sensor, resulting in less light on the sensor.

The *Field Of View* (FOV) of the imager is defined as the angle where incoming light is detected. FOV is given by the aperture, which limits the extent of the scene imaged. In Earth imaging cameras, it is usually the detector that limits the FOV of the imaging system.

## Grating

A key optical element in the design of a pushbroom hyperspectral imager is the grating. There are several types of gratings, and they can also be used in combination with prisms. A *diffraction grating* consists of a number  $N$  of single slits, with the width  $b$  of each slit, placed with an equal spacing  $a$ . Each slit acts as a source, and creates a diffraction/interference pattern when light is transmitted through the grating. This pattern gives several maxima called intensity maxima for different orders. For the *zero order*, the maxima is given at the same location, described by the diffraction angle  $\beta$ , for all wavelengths. For the higher orders, however, the location of the maxima,  $\beta$ , varies with wavelength. Longer wavelengths, such as red light, have a greater angle than the shorter wavelengths, such as blue light. It is worth noting that this is opposite from the effect happening in a prism, where shorter wavelengths are more refracted than the longer wavelengths.

While the diffraction grating transmits light, the *reflective grating* reflects light. The plane reflective grating may be seen as a polished surface with parallel grooves, i.e. long narrow cuts. The grating is filled with narrow parallel mirrors, each mirror acting as a source. Thus the same interference pattern as for the transmitting grating is created when the reflective grating is exposed to light.

The *grating equation* is given as

$$n\lambda = a(\sin \alpha + \sin \beta), \quad (2.9)$$

where  $n$  is the spectral order,  $\lambda$  the wavelength,  $a$  the distance between the grooves,  $\alpha$  the incident angle, and  $\beta$  the diffracted angle of the light. This equation is based on an idealised grating, but can be used to calculate the theoretical diffracted angle in a system, and is highly useful when designing a hyperspectral imager.

The reflective surfaces may also be tilted at an angle  $\omega_b$ . This gives a *blazed grating*, where  $\omega_b$  is known as the blaze angle. The blaze angle introduces a shift of the diffraction pattern away from the zero order over to higher orders. The grating is most efficient when

$$\alpha - \omega_b = \omega_b - \beta. \quad (2.10)$$

The light is separated according to the grating equation when the diffraction pattern is shifted to higher orders. This is the principle used in hyperspectral imaging, as the separated wavelengths are focused onto different parts of the imaging sensor.

### Optical Diagram

The optical diagram of a spectrograph can be seen in Figure 2.4. As seen in the diagram, the light enters the front lens and is focused through the slit. Further it is directed onto the second lens which collimates the light before it reaches the grating. The dispersive element shown in this optical diagram may be a grating together with a prism, which sorts the wavelengths so that the centre wavelength is parallel to the optical axis. The light is then separated and focused onto the image sensor by the third lens. This makes the captured image a *spectrogram*, with spectral information in one axis and spatial information from the slit in the other.

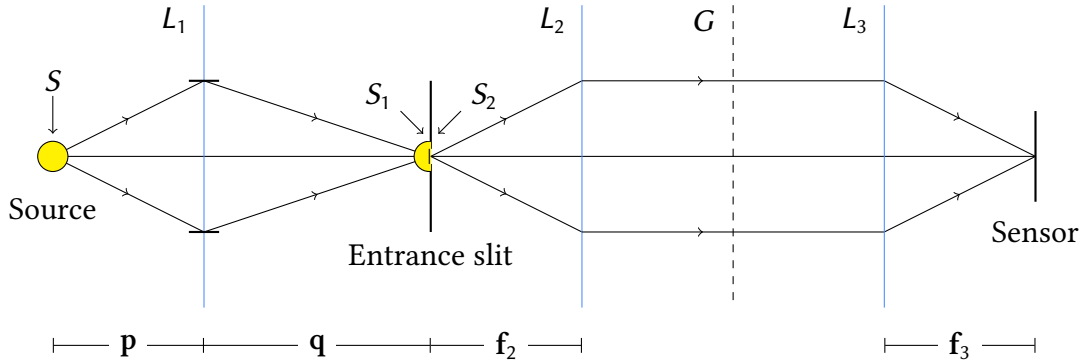


Figure 2.4: Optical diagram of a spectrograph.  $S$  is the area of the light source,  $S_1$  the area of the source image, and  $S_2$  the area of the entrance slit.  $L_1$ ,  $L_2$  and  $L_3$  are the lenses in the system, and  $G$  the grating element. Further,  $p$  is the distance between object and front lens,  $q$  the distance between front lens and projected image,  $f_2$  the focal length of  $L_2$ , and  $f_3$  the focal length of  $L_3$ . Based on figure found in [16].

### Geometrical extent

The *geometrical extent*, also known as etendue, characterises the ability of an optical system to accept light. It can be seen as an acceptance cone where the photons are allowed to travel, and defines how much light that can be detected by the instrument. The geometrical extent is defined as

$$G = \int \int dS d\Omega, \quad (2.11)$$

where  $S$  is the area of the emitting source and  $\Omega$  the solid angle. The geometrical extent is optimised when

$$G = \pi S \sin^2 \Omega = \pi S_1 \sin^2 \Omega_1 = \pi S_2 \sin^2 \Omega_2. \quad (2.12)$$

### Aberrations

In a perfect imaging system, all rays that originate from the same point in an object will cross at the same point in the system imaging plane. In real optical systems, however, this is not the case. This happens due to *aberrations*, which can be described in terms of how much a ray deviates from its desired location in the imaging plane. The desired location of the imaging points are based on first-order optics. Refraction of light follows *Snell's law*,

$$n_1 \sin \theta_1 = n_2 \sin \theta_2, \quad (2.13)$$

where the terms can be expanded so that

$$\sin \theta = \theta - \frac{\theta^3}{3!} + \frac{\theta^5}{5!} - \frac{\theta^7}{7!} + \dots, \quad (2.14)$$

where  $\theta$  is the angle measured from the normal of the boundary. For small values of  $\theta$ , the higher order terms can be neglected, and Snell's law can be written as

$$n_1 \theta_1 = n_2 \theta_2. \quad (2.15)$$

This, however, only holds for paraxial rays. For nonparaxial rays, higher order terms must be included. Including the third order term will give *third-order optics*, which introduces several types of aberrations such as coma, astigmatism and spherical aberrations.

### Sensor Detection

The Focal Plane Array (FPA), the detector matrix which the image is focused onto, converts the irradiance distribution produced by the imaging optics into the electrical signal recorded. It consists mainly of two parts: an array of detectors, and a multiplexer. The detector array produces an electrical response when hit by incident radiation. The multiplexer then collects the electronic response, and produces a signal with a digital representation of the detected image. The multiplexers are usually either Charge-Coupled Device (CCD) or Complementary Metaloxide Semiconductor (CMOS) switching circuits. The CMOS technology requires more circuitry within each unit cell, resulting in more noise in the sensor, but offers greater flexibility in the image readout than CCD.

### Quantum Efficiency

The *quantum efficiency*,  $QE$ , describes the spectral response of each pixel in the detector. It is defined as the fraction of photons that generates electrons detectable by the sensor. The

$QE$  can be calculated as a function of wavelength. This can further be used to characterise the sensitivity of the imager.

### Point Spread Function

The ideal wavefront entering an optical system for a point object will be spherical in nature, and will converge to a perfect point on the focal plane. However, imperfections in the optical system stop this from happening. Aberrations cause rays to land at different locations on the focal plane, and broadens the image of the point object. Distortions may cause the magnification to change as a function of image position. Absorption decreases the transmission of light through the system, and diffraction from the finite aperture size provides the final resolution. The actual focal plane image can be given by

$$E(x, y) = E_g(x, y) \star h(x, y), \quad (2.16)$$

where  $E(x, y)$  is the actual plane image,  $E_g(x, y)$  the true point source,  $\star$  represents a 2D spatial convolution operation, and  $h(x, y)$  is the Point Spread Function (PSF). An illustration of the PSF can be seen in Figure 2.5.

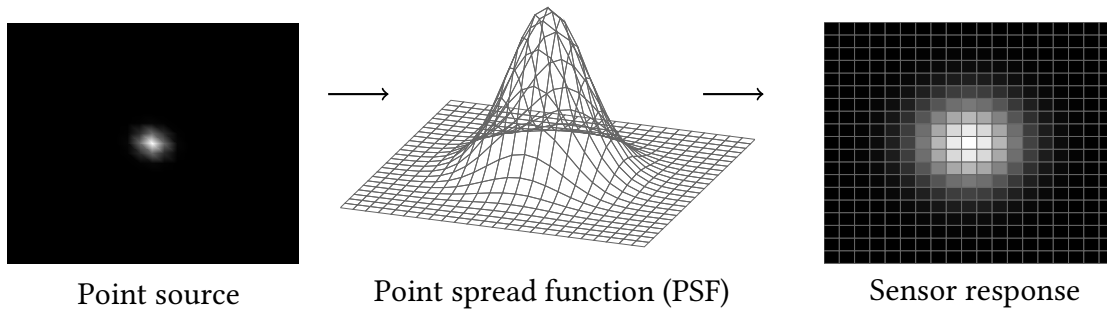


Figure 2.5: Illustration of the point spread function.

For a fuller understanding of the final optical design and performance of the system, the PSF should be characterised. This will give information about any geometrical aberrations in the system. Spatially scattered light, namely spatial stray light, may also be characterised by the point spread function [18].

## 2.2 Hyperspectral Imaging

Hyperspectral imaging, also known as imaging spectroscopy, is an imaging technique used to capture spectral information from a large number of spectral bands covering the same spatial area at approximately the same time. A hyperspectral imager can be based on several different designs. Among these are using a prism, a grating, or a combination of both, in the optical design to obtain spectral information, and further use the pushbroom or whiskbroom technique to obtain the spectral information for the full targeted area. Another option is to use a snapshot imager that captures the full hyperspectral cube at once using a sensor with many layers to obtain information from the different wavelengths at the same time as capturing 2D spatial information. Using filters is also an option, as seen in [19], or using filter wheels. One filter for each band becomes impractical quite fast, however, when moving from multispectral imaging with only a few spectral bands to hyperspectral imaging with potentially hundreds of bands. Filters and filter wheels are therefore more common in multispectral designs.

The pushbroom and whiskbroom concepts, as well as some other techniques, are further described in Section 2.2.1, while the data products obtained from hyperspectral imagers are described in Section 2.2.2. The theory presented is mainly based on [2], [16] and [20].

### 2.2.1 Remote Sensing Techniques

As previously mentioned, different techniques can be used to obtain the full hyperspectral cube when using hyperspectral imagers in remote sensing. Two common pointing methods are the pushbroom and whiskbroom scanning techniques, as illustrated in Figure 2.6 and 2.7, respectively.

The pushbroom technique is used when the imager is based on a design with the slit mounted in cross-track direction. One line in the targeted area, representing only one spatial direction, as spectral information is captured along the second axis, is captured at a time. The next line with new spatial information is then captured as the platform moves, as seen in Figure 2.6. These images are then stitched together to form a full spatial image, with spectral information along the third axis in the hyperspectral cube. When whiskbroom scanning is used, the slit is oriented in the along-track direction, and the scan happens in cross-track direction as the platform moves along-track. This allows the swath width to be decoupled from the velocity of the platform, but requires a more complex pointing system.

In [21] it is mentioned that the pushbroom design is favourable for EO purposes, as higher SNR may be achieved using the this technique compared to its whiskbroom counterpart.

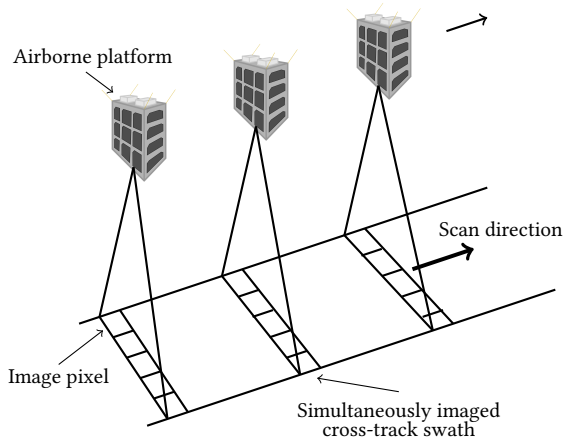


Figure 2.6: The pushbroom scanning technique. Based on illustration from [2].

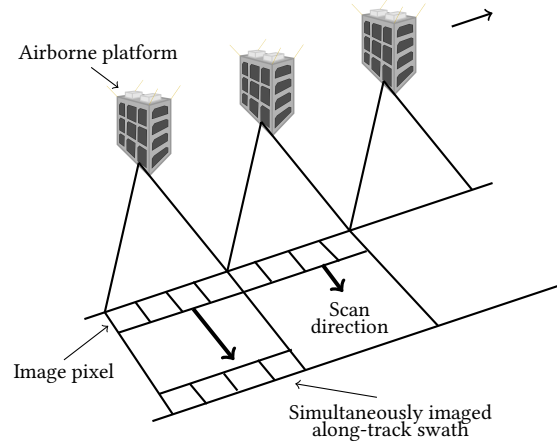


Figure 2.7: The whiskbroom scanning technique. Based on illustration from [2].

Other methods, such as the snapshot hyperspectral imager where the whole hyperspectral cube is acquired at one exposure, can also be used. Since the snapshot imager obtains the whole cube at every exposure, the only additional parameter needed is the exterior orientation, giving room for less geometric instabilities [22]. Another method using line filters, which makes it more applicable to multispectral imaging, is proposed in [19]. The imager has line filters on the imaging sensor to obtain spectral information from different bands. This is used in combination with the pushbroom technique to obtain full spatial images from all the bands used. This method can be hard to extend into hyperspectral imaging, however, due to the limited number of filters that can be fitted onto the sensor.

The imagers used in this report are based on the pushbroom design. Hyperspectral imagers using the pushbroom technique offer good enough SNR to be used in remote sensing, both in airborne and orbiting platforms. However, as mentioned in [23], high quality spectroscopic data is not necessarily easily obtained. The acquired spectrum may be distorted by artefacts that makes it harder to identify both spectral and spatial features. The method, however, requires a less complex pointing system than whiskbroom scanning, and the design of the imagers is less complex than for snapshot hyperspectral imagers.

### 2.2.2 Hyperspectral Data

When using the pushbroom technique, the data obtained is a series of frames stitched together to form a hyperspectral data cube. Each of these frames is a spectrogram, with spatial information along the  $y$ -axis, representing the slit height, and spectral information along the  $x$ -axis, as seen in Figure 2.8. The third axis of the cube represents spatial information in the moving direction of the platform, as seen in Figure 2.9.

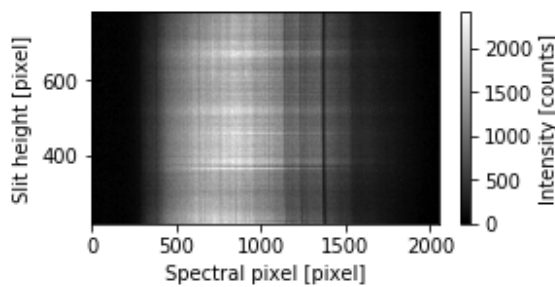


Figure 2.8: A spectrogram, with spectral information along the  $x$ -axis and spatial information in slit height direction along the  $y$ -axis, showing response from looking at a continuous lightsource.

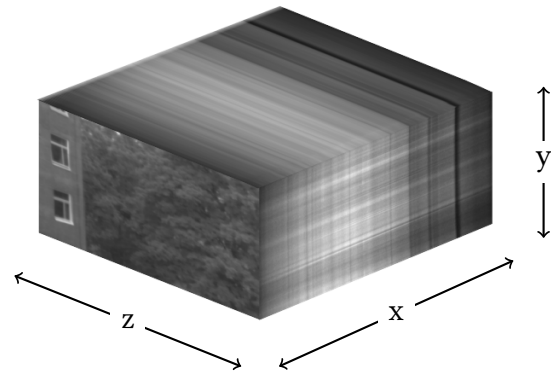


Figure 2.9: Illustration of a hyperspectral cube, with spectral information along the  $x$ -axis, spatial information in slit height direction along the  $y$ -axis, and spatial information in the moving direction of the platform in the  $z$ -axis.

After the hyperspectral cube has been formed, *spatial frames*, frames containing spatial information in both directions, can be extracted for selected wavelengths. Combining three such frames containing data from a red, a green and a blue wavelength, gives a familiar spatial coloured RGB image.

Calibration and characterisation of the imagers will be performed on the spectrograms, before they are stitched together to form the hyperspectral cube. A *frame* will therefore further refer to a spectrogram, unless it is specified as a spatial frame.

## 2.3 Calibration

Calibration is in general performed to convert measured data into physical, and more meaningful, units. This is done by comparing a known measurement, a standard, with a measurement done by the instrument that is being calibrated. In this project, spectral and radiometric calibration are performed on hyperspectral imagers. These calibration methods are further explained in Section 2.3.1 and Section 2.3.2, respectively.

Instruments used in remote sensing should also be calibrated in-flight or in-orbit, in addition to laboratory calibration [15]. Only the latter is handled in this report.

Further, it is worth noting that radiometric calibration assumes that the information from spectral calibration is known [15]. The spectral calibration must therefore be performed before the radiometric calibration can take place [16].

### 2.3.1 Spectral Calibration

In *spectral calibration*, or wavelength calibration, the relationship between wavelength and pixel position is determined. This can be achieved by using a monochromator that produces monochromatic light at controllable wavelengths, so that the response at every wavelength can be recorded. This method, however, is impractical, and also unnecessary, as the spectral-spatial distortion often is a somewhat well-behaved function. [2] Instead, a selection of light sources with known spectral peaks can be used to measure the response at some wavelengths, giving enough information to derive an approximation for the wavelength and pixel position relationship.

Spectral calibration can be performed using different set-ups. Among these are calibration using spectral lamps, a monochromator, or tunable laser technology. They all use known emission lines, or gas cells using known absorption lines, for calibration [15]. The method used in this report is calibration using spectral lamps. For this method, spectral lamps with known spectral emissions are used together with a diffuser, such as a diffuse board or an integrating sphere, to make sure the full FOV is uniformly filled with light.

The data from spectral calibration can also be used to characterise the spectral resolution of the system by finding the spectral bandpass, as described in Section 2.5.1, or to investigate the smile effect, described in Section 2.4. If there is a great amount of uncorrected smile in the system, spectral calibration coefficients should be found as a function of slit height.

### 2.3.2 Radiometric Calibration

The *throughput*, the usable flux at the sensor plane, depends on the input flux and the geometrical extent of the imaging system. It also depends on the quality and efficiency of the optical components used in the instrument [16]. Both the throughput and efficiency of the optical components can be calculated theoretically to find the total throughput and efficiency of the system. But for practical purposes it is more useful to calibrate the instrument against a source of known intensity to obtain the number a digital counts, or Digital Number (DN), registered by measuring the light emitted from a known reference source, and thereby find the relationship between detected signal and actual radiance. This is known as *radiometric*, or sensitivity, calibration.

The aim of radiometric calibration is to correctly convert the raw data from DN to radiance or reflectance, which are more physically meaningful units. This calibration can also remove some of the deviations caused by the hyperspectral sensor itself, such as erroneous pixels or dust in the system. If the radiometric calibration is performed in-flight or in-orbit, it can also make corrections for some of the atmospheric effects affecting the measurements [22].

The calibration factor for each pixel, or ratio between absolute units and counts, is given as

$$K = \frac{L}{C} \left[ \frac{\text{mW}}{\text{m}^2 \text{ sr nm counts}} \right], \quad (2.17)$$

where  $L$  is the radiance, depending on wavelength, in absolute units, and  $C$  is the background corrected sensor counts of the radiometric source [24]. To obtain the background corrected sensor counts, the dark current,  $b_0$ , must be removed from the raw image count. The dark current is the number of counts detected in the sensor when there is no light, and may arise due to thermal emission from within the optics, or leakage current in the photodetector, among others [25].

The goal of the radiometric calibration is therefore to determine the calibration coefficient  $K$ , and use the background corrected sensor counts to convert DN to the correct radiance value at each pixel. It is important to determine the calibration coefficient against an absolute radiometric reference, as this conversion is critical for the radiometric accuracy of the imager [25]. The dark current must either be characterised before the radiometric calibration can take place, or be made a part of the radiometric calibration procedure.

Radiometric calibration can be divided into two categories: *absolute* radiometric calibration, and *relative* radiometric calibration. This report focuses on the absolute radiometric calibration, which uses a known source to convert from the sensor output to absolute quantities. The relative radiometric calibration calibrates the imager by using observations from the same imager at different points in time, and comparing pixels to improve the image quality and uniformity [15].

To perform radiometric calibration, an irradiance standard lamp-integrating sphere, a standard detector-integrating sphere, a spectral radiometer-monochromatic parallel light, or a standard detector-diffuser, are among others equipment that can be used [15]. The method used in this report uses the irradiance standard lamp-integrating sphere set-up, which is explained further in Section 3.3. A diffuse reflective surface is also needed to make sure that the full FOV of the instrument is illuminated uniformly.

The data from radiometric calibration can also be used to characterise the linearity of the sensor response, and the stability of the response [15]. If the detector suffers from nonlinearities in the response, this nonlinearity should be characterised and corrected before the radiometric calibration is performed [26]. Linear systems are, however, easier to calibrate and characterise, as mentioned in [27], and are therefore preferable.

### **Traceability**

*Traceability* is the possibility to trace the measurement back to a trustworthy reference of the measured quantity. Spectral standard light sources might emit light at specific wavelengths due to fixed physical principles. But radiance light sources need to be calibrated with respect to primary standards before they can be used for radiometric calibration. Primary standards are operated and provided by national meteorological institutes such as the National Institute of Standards and Technology (NIST) [3]. A lamp certificate should therefore be given as a part of the information about the lamp used for radiometric calibration.

## 2.4 Smile and Keystone

Hyperspectral imaging instruments often suffer from spectral and spatial misregistrations. These effects may appear due to aberrations and misalignments in the optical system, which may distort the spectral signatures of the targeted object, and cause other nonphysical spectral signatures to appear in the data. This may lead classification algorithms to fail when trying to classify different objects, thus reducing the detection and classification accuracy of the algorithms. [23, 28] The quality of hyperspectral data also depends heavily on spatial coregistration between bands. Even small coregistrations can lead to large errors in the measured spectrogram [29]. In a practical optical design, perfect coregistration will not be possible, however. Errors are introduced by aberrations, distortions, and diffraction, among others [30]. These errors should be characterised, and if possible corrections should be made to compensate for the effects they make.

There are several types of spectral and spatial misregistrations that may appear in a distorted image. An illustration of the effects from some of these misregistrations can be seen in Figure 2.10. In an ideal system, all the lines in the figure should be straight and follow the grid. The circles represent the PSF, which is described in Section 2.1.2. The shape and size of the PSF may vary as a function of wavelength, but for each wavelength it should ideally keep the same size and shape. The letters *B*, *G*, and *R*, in the figure represents short, middle and long wavelengths within the spectral range, respectively.

As mentioned in [31], a typical spectral misregistration is *smile*, which is change in the central wavelength in a spectral channel as a function of slit height. This can be observed as a bent line in the spectrogram, and is illustrated by the blue circles on a curved vertical line in Figure 2.10. Furthermore, a typical spatial misregistration is *keystone*, which is a change in the position of the same spatial pixel in the scene as a function of wavelength. This effect makes the spectrogram look a bit skewed, and can be seen in Figure 2.10 as the three topmost circles being on a skewed horizontal line. Keystone can be caused by a difference in slit magnification with wavelength [21]. In short terms, as described in [32], smile is the curvature distortion of the spectral lines, while keystone is the distortion of the focal plane rectangle into a trapezoid.

Figure 2.10 also shows two other effects. The *G* column shows a variation of the width of the circles, which shows that the PSF may vary with spatial location in the image. The bottom row, on the other hand, shows an increasing height in the PSF as a function of wavelength. This can be caused by diffraction, and can be hard to avoid in a diffraction based system.

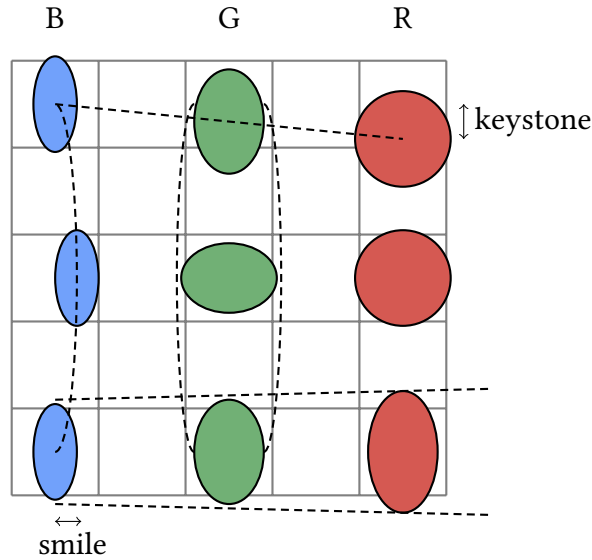


Figure 2.10: Illustration of different types of misregistrations that may occur in a pushbroom hyperspectral imager. Inspired by illustration in [23].

The tolerance for all of these errors is at the level of a small fraction of a pixel; less than 2% of a pixel for smile, and less than 5% of a pixel for the keystone effect are suggested in [27].

Ideally, all of the effects shown in Figure 2.10 should be characterised. This can be accomplished by measuring the PSF. To measure the PSF along the slit to cover all spatial positions for all wavelengths requires a most likely complex and dedicated set-up. An example of such a set-up can be found in [29], where the Line Spread Functions (LSFs) are measured in different directions to reconstruct the PSF. The focus in this report, however, is to detect mainly the smile and keystone distortions, while a set-up for measuring the PSF will be a part of the future work of this project.

A metric for characterising coregistration errors, including smile and keystone, is proposed in [30]. The metrics are essentially the integrated difference between the point spread functions, and it is shown that these differences correspond to an upper bound of the error in the image data. Using this metric, two commercial hyperspectral imagers were tested and compared in [33]. This showed that characterising imagers using the proposed metric in [30] made it possible to compare the performance of hyperspectral imagers more thoroughly, giving better estimates on the differences between them. This metric will not be used in this report, as the PSF will not be characterised, but it should be investigated further and used after the PSF has been measured.

### 2.4.1 Detection

There are several ways of detecting smile and keystone. Some methods detect only one of the effects at the time, while other methods may detect them both simultaneously. The key element for detecting smile is sharp spectral lines. These can be obtained using spectral light sources such as the spectral lamps used in spectral calibration. For detecting keystone, however, a sharp pattern in focus across the slit height is needed.

For remote sensing instruments, smile can be detected in-orbit by estimating the distortion of atmospheric absorption lines in the spectrum [34].

#### Detection of Smile and Keystone Separately

Examples on how to measure smile and keystone separately can be found in [21]. To detect smile, the slit was illuminated by spectral lamps at specific wavelengths and imaged on the focal plane. A diffuser was used to make sure that the illumination of the slit was uniform. Simple calculations were then performed on the centre of each spectral curve in every line of the spectrogram, and the result plotted as trend lines. A straight line would mean no smile, whereas a curved line would indicate smile, or similar distortions. Smile was then defined as the deviation from straightness of the monochromatic image of the slit, and measured as the maximum difference in the x-coordinate of the PSF centroid.

For measuring keystone in [21], a pinhole illuminated uniformly by a tungsten-halogen lamp was imaged. The result was a spectrum forming a line along the spectral axis in the spectrogram. The position of this bright line was then found for each spectral pixel, and the tilt, deviating from a straight horizontal line, would give indication of the keystone in the system. This was done for several positions of the pinhole along the slit height, and interpolation was then used to find trends for various positions along the slit. Keystone is often measured as an absolute length value, or as a fraction of a pixel in the image.

#### Detection of Smile and Keystone Simultaneously

However, in [32] it is stated that the smile and keystone effects should be detected and corrected simultaneously, since the imager projects spectral information along one axis of the sensor, and spatial information along the other axis at the same time. This can be achieved using Geometric Control Points (GCPs). This method is based on creating and finding known control points in the image, and determine the smile and keystone effects using these points. The GCPs are a function of the optical errors in the system, and must

therefore be uniquely determined for each imager. This method further maps the distinct points in the image to known reference points, as described in [20]. The distortion in the original image determined by the GCPs can be described by a two-dimensional quadratic polynomial distortion model, which is given as

$$\begin{aligned} x &= a_{00} + a_{10}x_{\text{ref}} + a_{01}y_{\text{ref}} + a_{11}x_{\text{ref}}y_{\text{ref}} + a_{20}x_{\text{ref}}^2 + a_{02}y_{\text{ref}}^2 \\ y &= b_{00} + b_{10}x_{\text{ref}} + b_{01}y_{\text{ref}} + b_{11}x_{\text{ref}}y_{\text{ref}} + b_{20}x_{\text{ref}}^2 + b_{02}y_{\text{ref}}^2, \end{aligned} \quad (2.18)$$

where  $x$  and  $y$  are the measured coordinates,  $x_{\text{ref}}$  and  $y_{\text{ref}}$  are the known reference coordinates, and  $a$  and  $b$  the model coefficients. This can be written in matrix form as

$$\begin{aligned} \mathbf{X} &= \mathbf{W}\mathbf{A} \\ \mathbf{Y} &= \mathbf{W}\mathbf{B}, \end{aligned} \quad (2.19)$$

where  $\mathbf{W}$  is an  $N \times M$  matrix, with  $N$  being the polynomial degree, and  $M$  the number of GCPs.  $\mathbf{X}$  and  $\mathbf{Y}$  are matrices the size of the image frame, holding the x- and y-coordinates, respectively, while  $\mathbf{A}$  and  $\mathbf{B}$  are matrices holding the model coefficients. Adding error terms gives

$$\begin{aligned} \mathbf{X} &= \mathbf{W}\mathbf{A} + \epsilon_x \\ \mathbf{Y} &= \mathbf{W}\mathbf{B} + \epsilon_y, \end{aligned} \quad (2.20)$$

where  $\epsilon_x$  and  $\epsilon_y$  are the error terms for  $x$  and  $y$ , respectively. The pseudo-inverse solution is then found as

$$\begin{aligned} \hat{\mathbf{A}} &= (\mathbf{W}^T\mathbf{W})^{-1}\mathbf{W}^T\mathbf{X} \\ \hat{\mathbf{B}} &= (\mathbf{W}^T\mathbf{W})^{-1}\mathbf{W}^T\mathbf{Y}. \end{aligned} \quad (2.21)$$

The model coefficients  $\hat{\mathbf{A}}$  and  $\hat{\mathbf{B}}$  are then, after they are found, used to describe the distortion model which is used when making corrections for the effects. To estimate the smile and keystone effects in [32], simple linear regression for keystone, and quadratic regression for smile, was performed on the data from the centre of the sensor.

A different method is presented in [34], where detection and correction of smile and keystone were done using the Phase Correlation (PC) method. Only observed data was used, unlike data from the lab in [32], which means that this method is suitable for post-launch characterisation and correction. Two subpixel image registration methods, Normalised Cross Correlation (NCC) and PC, were used to detect artefacts in the data, and the results

compared. To estimate smile, a quadratic approximation was once again used, while a linear approximation was again used for estimating the keystone effect. Spectral distortion estimated by the NCC method was smaller than the true distortion in the image, while the PC method was shown suitable for accurate and robust smile estimation. The PC method was also used to estimate keystone, and the method validated by the disappearance of keystone after correction.

### **Obtaining Data for Detection**

The calibration facility for airborne imaging spectrometers, CHB at DLR, uses a collimator set-up for geometric measurements, as described in [14] and [35]. For across-track measurements, the slit is mounted tangentially on a wheel so that an illuminated line is formed on the detector array by different wavelengths. Measurements are then performed by moving the line using a folding mirror. For along-track measurements the slit is mounted radially on a wheel, and measurements are obtained by turning the slit wheel. This set-up can also be used to find the LSF, among others, which may further be used to estimate the PSF, as done in [29]. As mentioned previously, a full set-up for characterising the PSF is outside the scope of this report. A smaller and simplified version of this collimator set-up is therefore proposed in this project, and is further described in Section 3.1.2.

In [32] an integrating sphere, mercury-argon and krypton calibration lamps, and thin vertical lines printed on a transparent film with 1 mm distance apart were used to create a spectrogram with detectable GCPs. The spectral calibration lamps were used together with the integrating sphere to generate known spectral lines across the full spatial length of the imager slit. The vertical lines were then placed between the imager and the integrating sphere so that the known interference pattern was imaged. The resulting spectrogram was then used to determine the GCPs. To minimise random noise, 36 images were acquired and averaged before further analysis.

### **2.4.2 Correction**

Corrections can be made in hardware by changing to higher quality lenses with less distortions, making the whole imaging system better aligned, or by making other improvements to the design. These methods work for larger errors, but when the errors get smaller, making the corrections in hardware gets more difficult. Developing a perfect imaging system is by no means practical, and some distortions will most likely always be present. In [31], resampling, thus making the corrections in software, is proposed as an

alternative method to correcting keystone in hardware. For high-resolution sensors it was found that better corrections could be made using resampling than what was possible by making the correcting in hardware. Using resampling for making corrections for the smile effect was also suggested.

When using the GCP method as described in [32], the model coefficients  $\hat{\mathbf{A}}$  and  $\hat{\mathbf{B}}$ , once found, can be used in Equation 2.19 to transform the coordinates in the reference image into non-integer coordinates in the measured image frame. Resampling can then be used to interpolate between the integer pixel locations in the measured frame to obtain the measured values for the new non-integer measured frame coordinates. The corrected image is then created by filling in the value at each reference location with the value from the corresponding measured coordinates. By using this "reverse" technique, overlapping pixels and holes are prevented. Using this method allows correction for smile and keystone to be done simultaneously. A cubic regression was found to produce the best fit without overfitting the data. After the correction had been applied, the mean errors were all significantly reduced, with better results towards the centre of the detector. Errors were found to increase significantly below 420 nm and above 840 nm.

In [34], cubic spline interpolation was used to correct the artefacts, due to its good trade-off between smoothness and shape preservation, as described in [36].

### 2.4.3 Requirements

Past studies have shown that high sensor accuracy is important when obtaining data, if it is to be useful for scientific research [34]. A spectral uncertainty of less than 1% of Full Width at Half-Maximum (FWHM) throughput of the spectral response function is found necessary in [37], and a maximum spatial misregistration of 5% of the pixel size is found in [23]. In [27] less than 2% of a pixel for the smile effect, and less than 5 % of a pixel for the keystone effect is suggested. For remote sensing systems these properties may change after launch, which makes in-flight or in-orbit correction of these effects an important issue that should be handled for these systems [28].

## 2.5 Other Effects

In addition to smile and keystone in the system, there are several other effects and system parameters that can, and should, be characterised. A number of possible characteristics of the hyperspectral imager are mentioned in [25], while a set of effects especially important for ocean colour sensor are presented in [13]. Among these are characterisation of effects such as polarisation sensitivity, stray light, temperature dependence, noise and so on, as well as system parameters such as spectral range, spectral bandpass, linearity of the sensor response, signal-to-noise ratio, the dynamic range and an instrument model.

This section gives a further description of the spectral bandpass, linearity of the sensor response, signal-to-noise ratio, polarisation sensitivity, stray light, and temperature dependency. Only the spectral bandpass and the linearity of the sensor response are characterised in this report, but the other effects mentioned in this section should be also characterised in the near future, together with the PSF described in Section 2.1.2.

### 2.5.1 Spectral Bandpass

The *spectral bandpass*,  $BP$ , is defined as the recorded FWHM of a monochromatic spectral line, and is a measure of the instruments ability to separate adjacent spectral lines in the spectrogram [16]. An illustration of the FWHM for a well aligned and a more realistic instrument can be seen in Figure 2.11.

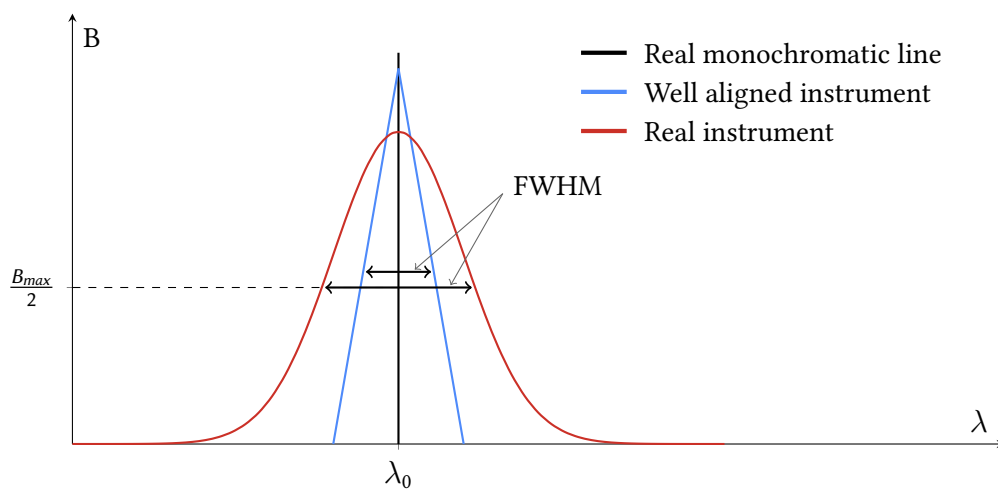


Figure 2.11: Illustration of bandpass, Full Width at Half Maximum (FWHM), for a well aligned and a real instrument. Based on illustration from [16].

The spectral bandpass, or wavelength spread across the sensor, can be calculated as

$$BP = FWHM \approx \frac{d\lambda}{dx} \times w' \quad [\text{nm}], \quad (2.22)$$

where  $d\lambda/dx$  is the linear dispersion describing the change in incremented wavelength per sensor distance, and  $w'$  the exit slit width.  $BP$  can also be expressed using the entrance slit width, as

$$BP = \frac{a \cos \alpha}{n f_2} \times w \quad [\text{nm}], \quad (2.23)$$

where  $w$  is the entrance slit width,  $a$  the distance between the grooves in the grating,  $\alpha$  the angle of the incident wave,  $n$  the spectral order, and  $f_2$  the collimator focal length. [16]

In [27] it is stated that a spectral bandpass of 10 to 20 nm should be sufficient to record the spectral absorption and scattering characteristics of the range of materials found on the Earth's surface, for remote sensing instruments. In [13] it is suggested that FWHM should be known with an accuracy of about 0.5 nm.

### 2.5.2 Linearity of Sensor Response

The linearity of the sensor response is normally good in the relevant types of photodetectors used in hyperspectral imagers [25]. The linearity should, however, be measured, to make sure that no significant nonlinearities in the sensor response are present. If the uncertainties in the measurements are larger than the nonlinearity of the sensor response, a linear relation can be used between the sensor count and actual radiance in the radiometric calibration [13]. If not, the nonlinearities in the sensor response must be characterised and then further handled during the calibration.

### 2.5.3 Signal-to-Noise Ratio

The SNR of the imager can be calculated using the noise of a single detector element when viewing a constant light source, and must be determined for each spectral band used. If possible, the SNR should also be determined at various light levels within the dynamic range. This is often done at the same time as characterising the dynamic range, as the same data can be used for both characteristics. [13]

### 2.5.4 Polarisation Sensitivity

Polarisation effects is an unwanted feature, but most instruments will display some sensitivity to the polarisation state of the radiance they observe [38]. The sensitivity may be introduced by various optical effects, such as metallic diffraction gratings, and will only affect the image if the incoming light has a significant degree of polarisation [25]. It may therefore not occur at all times, and is thus not removed by the various calibrations, which only remove static effects [39]. Even though the errors induced by polarisation sensitivity are small, the effects are still evident when testing atmospheric correction algorithms with polarisation present in the radiance observed [38].

Characterising the polarisation sensitivity of imaging systems used in remote sensing is especially important when observing ocean colour, as the light is both scattered, absorbed, reflected, and refracted when travelling through the atmosphere, interacting with the ocean surface and below, and up through the atmosphere again before reaching the imaging sensor, making the light observed on top of the atmosphere highly polarised in certain directions [40]. Both the radiance and polarisation also varies with wavelength, making it necessary to characterise the sensitivity of the full spectral range of the imager. The polarisation sensitivity may be reduced to a sensitivity level down to below 0.5% by using a polarisation scrambler [13]. Higher levels of polarisation sensitivity may be removed by firstly characterising the sensitivity of the instrument, and then estimating the polarisation of the incoming radiance. Corrections for the assumed polarisation present can then be made, as done in [38]. The characterisation accuracy should be of about 0.2% [13].

In [38] it is mentioned that only three elements are needed to study the effect of polarisation sensitivity of an instrument, which can be found by illuminating the instrument with linearly polarised light in three different ways. The polarisation properties of the observed radiance on top of the atmosphere is mainly determined by Rayleigh scattering, and also aerosol scattering for higher wavelengths such as 700 to 800 nm. This can be used in combination with atmospheric models to perform polarisation correction in conjunction with atmospheric corrections. A method for characterising polarisation sensitivity using a polarisation spectral assembly that produces linearly polarised light, containing an Ahrens prism and a collimating mirror, is presented in [39]. Another method presented in [13] uses an integrating sphere with a low degree of polarisation together with a linear polariser sheet with known polarisation characteristics that is placed between the sphere and the imager. The polariser sheet is then rotated at least 180°, but preferably 360° to confirm the results, and measured at intervals of about 15° to obtain the sensitivity measurements.

### 2.5.5 Stray Light

Stray light may be defined broadly as all the light that deviates from the ideal optical path in the optical system, and will mainly become a problem for the imaging sensor when it makes light reach the wrong detector element [13]. There may be several different sources causing stray light. Light that originate from outside of the sensor's FOV, called *out-of-field stray light*, is one of the major sources. Stray light may further be separated into two classes: random and directional. *Random stray light* is typically due to scatter from different components within the system itself, such as mirrors or screws, and will be directly proportional to the flux density. *Directional stray light*, on the other hand, can result in more distinct errors, such as incorrect illumination due to overfilled optics, re-entry spectra of unwanted orders or stray light due to periodic machine ruling errors. [16]

The occurrence of stray light within an instrument is a well-known problem in remote sensing instruments, as mentioned in [18], and typically arises when the instrument measures a source quite different from the calibration source. For example, large radiometric bias error may occur when looking at high contrast scenes, such as bright clouds over dark oceans, in earth observation. When observing ocean colour, analysing how the dark regions are affected by stray light is especially important, and an essential criterion is to find how many pixels away from a bright region the stray light affects the dark region, as this determines the masking needed around clouds when processing ocean colour data [13].

Stray light is a natural part of any imaging system, and should therefore be characterised so that corrections can be made to reduce the stray light in the system. In general, stray light characterisation involves measuring high contrast scenes from a dark to a bright zone, or visa versa [13]. A simple method to correct both spectral and spatial stray light using correction matrices is presented in [18]. The spectral stray light correction is based on characterisation of the instrument's system-level stray light response by obtaining the Spectral Line Spread Function (SLFS). The SLFS is then divided by the total defined in-band signal, and the relative fractional amount of radiation incident on pixel  $j$ , that is scattered onto other elements in the detector array, is obtained by setting the pixels within the defined in-band area to zero. The relative fractional scattering function found is named the Stray Light Distribution Function (SDF), which is obtained for all wavelengths to form an SDF matrix, which then is further used for the spectral stray light correction. For correction of spatial stray light, a set of PSFs must be characterised. Each PSF is then used to derive an SDF, which in the spatial case is the ratio of stray light signal to the total signal within the field of the resolving power of the instrument. Interpolation is used between the SDFs to

form the SDF matrix, which then is used to correct the spatial stray light in the system. With accurate laboratory system-level characterisation prior to launch, these corrections can significantly reduce the out-of-band systematic errors, as well as errors arising from bright targets in a scene, in remote sensing instruments. [18]

A different method of stray light characterisation is presented in [41]. The PSF, also called the Glare Spread Function (GSF), can again be found by using a point light source in dark surroundings, and capture a huge set of data with the light shining into the camera from different directions. Another approach is described in [42], where the instrument looks into an integrating sphere with a light trap at the end. This is described as the single integrating sphere method, and accounts for light from both inside and outside FOV over the whole range of incident angles. Different positions of the light trap is then measured sequentially. This method represents objects at infinite distance. It is also mentioned in [41] that the best way to correct for flare is to minimise it by using the right materials, surface treatment and orientation, and production processes in the lens production.

Stray light should be characterised with an accuracy of 0.5%, and the stray light effects after correction should be less than half of that amount, according to [13].

### 2.5.6 Temperature Dependence

The temperature dependence of the system must be characterised prior to operation for the expected temperature range of the environment. Most detectors are highly sensitive to temperature variations, both in offset and gain, and mechanical structures may deform with temperature, introducing geometrical impact on the measurements. This makes investigation of temperature dependence especially important for satellite instruments, as these may experience great temperature fluctuations in-orbit due to both a yearly temperature cycle affected by the Sun-Earth distance, and a cycle driven by the temperature increase when receiving direct sunlight versus temperature decrease when positioned in the Earth's shadow. [13]

Characterisation of the temperature dependence can be accomplished using thermal vacuum chambers, where the whole instrument is at thermal equilibrium. This approach does, however, not capture the temperature gradients that will be experience in-orbit. A more accurate approach to reduce the sensitivity to temperature variations is by maintaining temperature control of the focal plane and the readout system during operation. [13]



## 3 | Methods

This chapter describes the different calibration and characterisation set-ups and procedures, and gives detailed information about the equipment used.

As mentioned in the previous chapters, calibration and characterisation are distinguished by their goals. Calibration identifies parameters holding metadata, such as the pixel to wavelength relationship in spectral calibration, and sensor count to radiance in radiometric calibration. It uses known sources for comparison, and the results are used to convert raw sensor data into physically absolute units. The characterisation identifies sensor parameters describing the capabilities of the system itself. It identifies characteristics, such as the spectral bandpass, and other features in the system. The results from the characterisation can also be used to identify distortions, such as smile and keystone, in the system.

There is assumed no atmospheric attenuation during the laboratory calibration and characterisation procedures. The distance between imager and light source is small, and there should therefore be close to no effect on the results when calibrating in the lab. Should the distance increase however, such as for in-flight or in-orbit calibration, handling atmospheric effect must be a part of the procedure.

### 3.1 Equipment

For both radiometric and spectral calibration, a 30 cm integrating sphere (Model ISS-30-VA, Gigahertz Optik), with 10 cm output port, was used as a spatially uniform target. For radiometric calibration, the installed integrating sphere tungsten halogen lamp was used as light source. The lamp certificate can be found in Appendix B, with the reference radiance mapped with 10 nm resolution. The interpolated reference radiance can be seen in Figure 3.1. For spectral calibration, spectral calibration lamps were inserted through an inlet in the sphere. Argon, krypton, xenon and mercury-argon calibration lamps (Newport Models 6030, 6031, 6033 and 6035, respectively) were used with a Newport 6044 AC power supply to provide calibration wavelengths from 400 to 900 nm. The emission lines with wavelength values of the lamps can be found in [43].

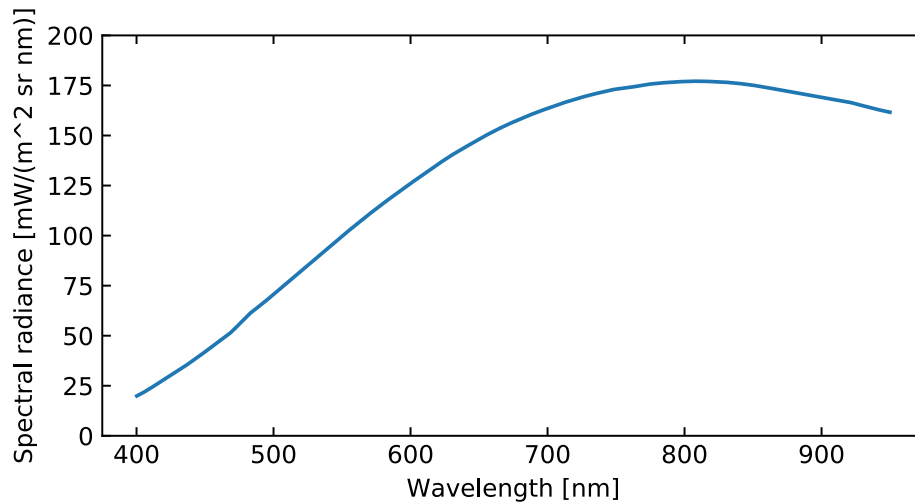


Figure 3.1: Reference radiance for the targeted spectral range, interpolated using cubic interpolation, for the integrating sphere tungsten halogen lamp source (ISS-30-VA).

### 3.1.1 HSI V4 and HSI V6

There are two hyperspectral imagers used in this report, the HSI V4 [44] and the HSI V6 [45], which can be seen in Figure 3.2 and 3.3, respectively.



Figure 3.2: Image of the HSI V4.



Figure 3.3: Image of the HSI V6.

The imagers were both developed by Fred Sigernes at UNIS, with the HSI V6 being the most recent version of the two. The specifications of the imagers can be seen in Table 3.1. They are both based on the same optical design, and uses camera heads from Imaging Development Systems (IDS), but they have different lenses and specifications. A general optical diagram for both imagers can be seen in Figure 3.4.

Table 3.1: Specifications of the HSI V4 and HSI V6.

| Part                      | HSI V4                                 | HSI V6                                 |
|---------------------------|--|--|
| Camera head               | UI-3360CP-NIR-GL R2                    | UI-3060CP-M-GL R2                      |
| Image size                | (1088, 2048)                           | (1542, 2056)                           |
| Spectral range            | 297.5 - 1005.5 nm                      | 400 - 800 nm                           |
| FWHM                      | 1.4 nm                                 | Approx. 3.3 nm                         |
| Grating                   | 600 grooves/mm<br>transmission grating | 300 grooves/mm<br>transmission grating |
| Slit height               | 3 mm                                   | 3 mm                                   |
| Slit width                | 25 $\mu\text{m}$                       | 50 $\mu\text{m}$                       |
| Slit height magnification | 1.28                                   | None                                   |

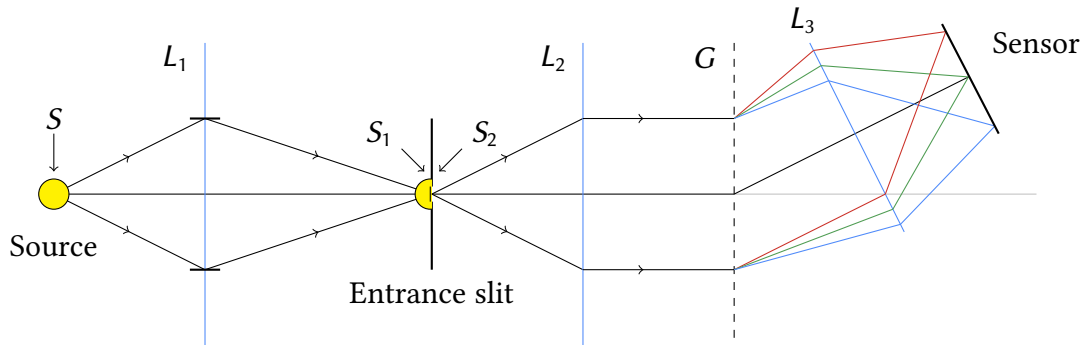


Figure 3.4: Optical diagram of HSI V4 and V6.  $S$  is area of the light source,  $S_1$  area of the source image, and  $S_2$  area of the entrance slit.  $L_1$ ,  $L_2$  and  $L_3$  are the lenses in the system, and  $G$  the transmission grating.

### 3.1.2 Collimator Set-up

A collimator set-up was designed to allow a pattern for detecting keystone to be in focus on short distances when the HSI is focused to infinity. The design was made since the imagers used in this report both are focused at infinity, as they will further be used in remote sensing applications.

The set-up consists of a collimator lens and a striped pattern, and is meant to be used together with spectral light sources to obtain data for both smile and keystone correction. The lens objective used as the collimator lens is a Zeiss Makro-Planar 100 mm f/2 lens with Nikon camera bayonet mount. A 3D printed lens cap was then made with a striped pattern on the top of the cap at a distance corresponding to the back focal length of the lens.

This allows the pattern to be seen as it is in infinity when looking through the front of the collimator lens. The pattern is in other words collimated when viewed from the front. The HSI was then placed right in front of the lens, and the pattern illuminated from behind. The set-up can be seen in Figure 3.5, and the striped pattern is shown in Figure 3.6.



Figure 3.5: The collimator set-up consisting of a Zeiss Makro-Planar 100 mm f/2 lens, and a 3D printed lens cap with top pattern.

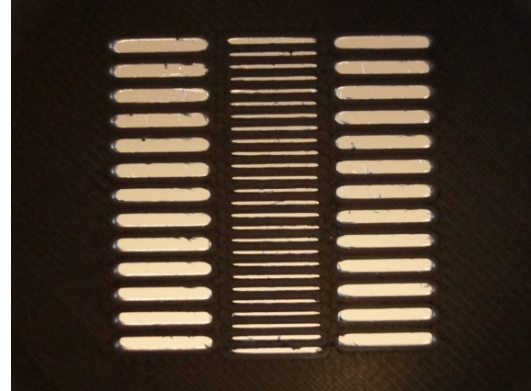


Figure 3.6: The 3D printed pattern, imaged using a Sony  $\alpha$ 57.

## 3.2 Spectral Calibration

Spectral calibration was performed as described in Appendix A.1, for both imagers. The gain was kept at zero (no gain) and the binning at one (no binning) at all times. The full Area Of Interest (AOI) was calibrated. Each dataset contained at least 20 images in the form of spectrograms.

The wavelength pixel relation is assumed to be a second order polynomial fit

$$\lambda \approx a_0 + a_1 \cdot p + a_2 \cdot p^2, \quad (3.1)$$

where  $\lambda$  is the wavelength in nanometres and  $p$  the spectral pixel index. The result after the data is analysed is the constants  $a_0$ ,  $a_1$  and  $a_2$  [16].

To calculate the calibration coefficients, the observed peaks were compared to the reference peaks for the belonging spectral light source. The reference peaks used were chosen among the useful wavelengths for the calibration lamps, given in [43]. The selected peaks for the argon and mercury-argon lamps can be seen in Table 3.2. In the analysis, only data from the argon and mercury-argon lamps were used, but the method can be extended to include data

from the other lamps as well. Argon and mercury-argon lines were chosen as they cover the full usable wavelength range of the imagers.

*Table 3.2: Chosen reference peaks for argon and mercury-argon used in spectral calibration.*

| Lamp   | Wavelength [nm] | Lamp | Wavelength [nm] |
|--------|-----------------|------|-----------------|
| Hg(Ar) | 404.66          | Ar   | 751.46          |
| Hg(Ar) | 435.84          | Ar   | 763.51          |
| Hg(Ar) | 546.07          | Ar   | 772.38          |
| Hg(Ar) | 576.96          | Ar   | 794.82          |
| Ar     | 696.54          | Ar   | 811.53          |
| Ar     | 706.72          | Ar   | 826.45          |
| Ar     | 727.29          | Ar   | 842.46          |
| Ar     | 738.4           |      |                 |

The analysis starts by analysing the data from the mercury-argon lamp, and compare the peaks in the centre horizontal line in the spectrogram to the reference peaks for mercury-argon, found in Table 3.2. The centre horizontal line is used to avoid the smile effect. A polynomial fit is then found, and the procedure repeated for all spectrograms containing mercury-argon peaks. The average fit coefficients are then used in the further analysis. Next, the argon data is introduced. Again, the spectrum from the centre horizontal line in the spectrogram is compared with the reference peaks, and the result is used to improve the polynomial fit coefficients found from the mercury-argon data. This is repeated for all argon spectrograms collected, and the average coefficients for the final fit are the result of the analysis. These polynomial fit coefficients correspond to the final calibration coefficients  $a_0$ ,  $a_1$  and  $a_2$ .

### 3.3 Radiometric Calibration

Radiometric calibration was performed as described in Appendix A.2, for both imagers. The gain was kept at zero (no gain) and the binning at one (no binning) at all times, and the full AOI was calibrated. As mentioned in Section 2.3.2, the calibration factor for each pixel  $K$  is given by Equation 2.17. The dark current,  $b_0$ , must either be characterised before the radiometric calibration, or be made a part of the radiometric calibration procedure. In this project, it was made a part of the calibration procedure. The radiometric calibration therefore consists of two steps: finding the dark current,  $b_0$ , and further finding the calibration coefficient,  $K$ , to obtain the full relation between sensor counts and radiance.

As described in Section 2.3.2, data from radiometric calibration can also be used to characterise the linearity of the sensor response, which is further investigated in 3.4.3. As mentioned in [26], any nonlinearities should be characterised before the radiometric calibration takes place. During radiometric calibration of the HSI V4, a greater data set was therefore collected for investigation of this effect. If the sensor response is nonlinear and this is not characterised, the radiometric calibration is only valid for the same settings as the settings used for the calibration data collected.

#### Dark Current Data

To estimate the dark current, the average dark current value in the whole frame was calculated, and the average value for all the frames collected was further used as the single value dark current estimate. A single value estimate was chosen over a full matrix estimate, as a uniform dark current distribution was assumed.

#### Radiometric Calibration Data

The calibration coefficient  $K$  for each pixel was found for all pixels in the image at the same time, resulting in a calibration coefficient matrix  $\mathbf{K}$  the size of the frame. The background corrected sensor counts of all pixels in the image,  $\mathbf{C}$ , was found by subtracting the dark current value from all pixels in the observed frame.  $\mathbf{C}$  was then divided by the exposure time to obtain a calibration coefficient directly applicable to data captured at different exposure times, assuming a linear sensor response. The reference data, sampled at only 10 nm resolution, was interpolated using cubic spline interpolation, and further expanded into a matrix the same size as the spectrogram by repeating the reference data varying with wavelength for every slit height position. The calibration coefficients were then calculated using Equation 2.17 for the full frame

$$\mathbf{K}_s = \frac{\mathbf{L}}{C_{\text{per } s}} \left[ \frac{\text{mW s}}{\text{m}^2 \text{ sr nm counts}} \right]. \quad (3.2)$$

The coefficients were calculated for all spectrograms collected, and an average coefficient matrix was used as the final radiometric calibration coefficient matrix.

## 3.4 Characterisation

The characterisation of hyperspectral imagers includes analysis of many different effects and system parameters. The main focus of the characterisation part in this report is determining the smile and keystone effects, as described in Section 2.4. Other effects characterised in this report are the spectral bandpass, and the linearity of the sensor response, which are described in Section 2.5.1 and Section 2.5.2, respectively. The methods used to investigate these effects are described in Section 3.4.2 and Section 3.4.3, while Section 3.4.1 is dedicated to the characterisation of smile and keystone.

### 3.4.1 Smile and Keystone

The method used for detecting and correcting the smile and keystone effects in the imagers is based on the method presented in [32], which is described in Section 2.4. The method uses GCPs, and allows both smile and keystone to be corrected simultaneously. Without GCP correction, individual calibration should be done to every pixel of the FPA due to possible nonlinearities across the FPA. Using GCPs to correct the image therefore greatly reduces the complexity of the overall calibration procedure [32].

The first step was to create a spectrogram with distinguishable points in it, to be able to identify the coordinates of the created points. In [32], spectral calibration lamps were used to create spectral lines, and thin vertical lines printed on transparent film were placed in front of the entrance slit to create a known interference pattern along the detector. The intersection points of these lines were used as the GCPs. The same idea was used for the characterisation done in this report. Spectral calibration lamps were used to create spectral lines in the image, while the pattern shown in Figure 3.6 was used together with the collimator set-up described in Section 3.1.2 to create sharp lines in the across-slit direction of the imager, focused in infinity. The intersection points created by these lines were then further used as the GCPs.

Data for smile and keystone detection in the HSI V4 was collected as described in Appendix A.3, except maximum aperture on the collimator lens was used instead of as small aperture as possible while still covering the full FOV of the imager, as described in the procedure. The HSI was placed so that it looked into the centre of the collimator lens, as seen in Figure 3.7, to image the most narrow slits shown in Figure 3.6, which were illuminated from the other side by spectral calibration lamps. Data was collected using both argon, krypton, xenon,

and mercury-argon spectral lamps, that were used together with the integrating sphere to ensure uniform illumination. At least 30 images were collected for each spectral lamp, to minimise random noise by averaging later in the analysis.

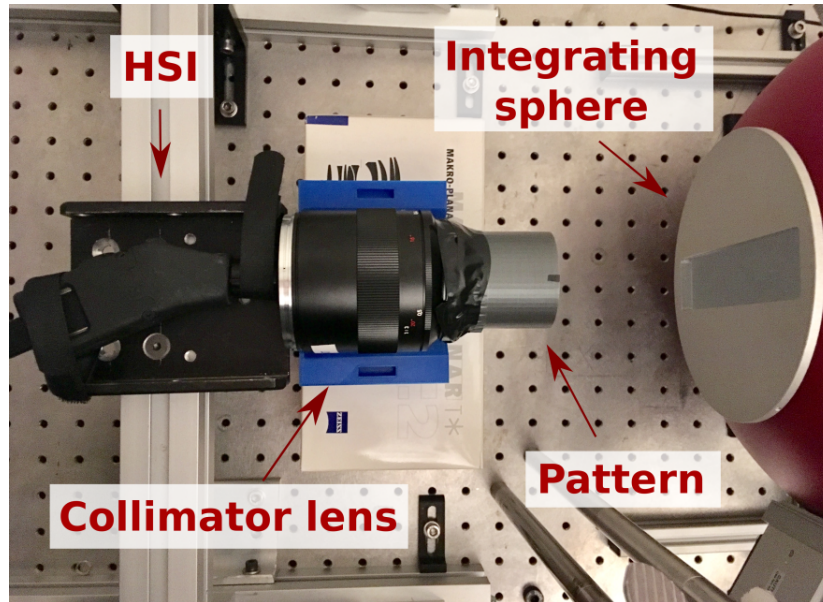


Figure 3.7: The collimator set-up with the HSI V4 in the lab. The HSI V4 looks into the centre of the collimator lens, and the whole set-up points towards the integrating sphere outlet.

After data was acquired, it was analysed using the methods found in [32]. The main idea is based on using known ground control points, made up by the intersection points between the spectral lines in the spectrogram made by the spectral lamps, and lines in the spatial direction made by the striped pattern. The placement of these points is detected to create a distortion model, and to estimate the smile and keystone effects. Since the true location of the ground control points are known, a reference grid containing the true locations is made. The distortion model is then used to find the coordinates in the measured frame for all the coordinates in the reference grid, and values from the measured frame are filled into the reference grid, thus creating the corrected frame.

The location of the GCPs were detected by first locating the peak of the spectral lines for all slit heights, then further detecting every dip in the spectral lines created by the striped pattern. The points were then evaluated as good or bad points based on number of points in their line, and distance from expected position when comparing spectral and spatial position with other points on the same spectral or spatial line. Limits were set, and bad points removed from the list of usable GCPs.

Estimation of the smile effect was done by using all of the GCPs found in each spectral line and make a second order polynomial fit to each line. The curve of each line was then be plotted, and the curve would indicate the amount of smile in the system. In [21] smile was defined as the deviation from straightness in the spectral line, measured as the maximum difference in spectral direction of the centre of the line. The same measure was used to quantify the smile effect in this project. Keystone in the system was estimated by making a linear fit of the position of all the GCPs in each spatial line. The keystone effect was then quantified as the number of pixels shifted from first to last pixel in the spatial direction.

When quantifying the smile and keystone effects, only the GCPs giving smile and keystone values within the average value plus/minus the standard deviation were kept as good points. Any points outside these requirements were removed from the GCP list and no longer used. New averages estimating the smile and keystone effects were then calculated and used as quantitative values.

To make a suitable reference grid, the GCPs in the centre of the spectrogram were used, as these were assumed to have the least amount of distortions. All GCPs in the spectral line closest to the centre were used to find the reference positions for the striped pattern, while the GCPs in the spatial line closest to the centre were used to get the positions of the reference points in the spectral direction.

After the reference points were found, they were used together with the GCPs to find the model coefficients  $\hat{\mathbf{A}}$  and  $\hat{\mathbf{B}}$  in the distortion model, using Equation 2.21. The coordinates for the reference points in the measured frame were then calculated using the model coefficients and the reference coordinates in Equation 2.19, resulting in new non-integer coordinates. Interpolation was therefore used to obtain the measured values for these non-integer positions, and the values were then mapped to the new reference frame to create the corrected image. To speed up the mapping process, the coordinate transformation was done using sparse matrices, as described in [46].

### 3.4.2 Spectral Bandpass

The bandpass was calculated using data from the spectral calibration. The bandpass was found for one peak at the time. The maximum intensity of the peak was first detected using the function `find_peaks()`, and the width of the peaks found using the function `peak_widths()`, both from the Python `scipy.signal` package. The pixel indices of the start and end of the peak width was found and converted to wavelength values,

using the spectral calibration coefficients, to find the full width in nanometres. This was repeated for every peak detected in about 30 frames with argon peaks and 30 frames with mercury-argon peaks for each of the imagers. The values were then averaged to give an estimate of the spectral bandpass. The average value for the 546.07 nm mercury-argon line was also estimated, as this wavelength is close to the designed centre wavelength of the system, which is at about 553 nm for the HSI V4 [44], and is therefore expected to be sharp with low FWHM.

### 3.4.3 Sensor Response

As mentioned in Section 3.3, a greater data set, using a predefined set of different exposure times, was collected during data collection for radiometric calibration of the HSI V4. This data was further used to investigate the linearity of the sensor response. The relation of dark current values as a function of exposure time was also investigated.

#### Dark Current

The average dark current response in the middle line of the spectrograms captured at different exposure times were analysed and compared. The average dark current value in each middle line was also calculated, together with the standard deviation of this value, and a linear fit found to describe the relationship between average dark current count and exposure time.

#### Radiometric

When investigating the radiometric response as a function of exposure time, the middle line of the spectrogram was again used. The average middle line response at different exposure times was calculated, and compared. The average middle line response divided by exposure time was also calculated and compared, to show the detected response per ms.

## 4 | Results and Discussion

As mentioned in [32], results from analysing hyperspectral data are often hard to present due to the size and complexity of the hyperspectral data cube. Some results are therefore presented using graphs, others displayed as images.

The first goal of this project was to set up spectral and radiometric calibration procedures, and calibrate hyperspectral imagers using the existing equipment at NTNU. Both spectral and radiometric calibration procedures were designed, and can be found in Appendix A. The calibrations were then performed on the HSI V4 and HSI V6. Results from the spectral and radiometric calibration for both imagers are described in Section 4.1 and Section 4.2, respectively.

The second goal was to investigate a method for detecting smile and keystone effects in the system, and further make corrections for these effects. A method detecting and correcting both smile and keystone simultaneously, using ground control points, was found in [32]. A set-up consisting of a collimator lens and a striped pattern was designed to create a spectrogram with identifiable ground control points, and the algorithms presented in [32] were then implemented. The smile and keystone correction was done using data from the HSI V4, and the results are presented in Section 4.3.1.

Further, it was found that the data collected during spectral and radiometric calibration could be used to characterise other effects in the system, such as spectral bandpass, the dynamic range, and linearity of the sensor response, among others. Spectral bandpass was estimated in this report, and the result can be found in Section 4.3.2. The linearity of the sensor response was also investigated, and the results presented in Section 4.3.3.

Both the HSI V4 and HSI V6 has a slit height of 3 mm, while the optical design allows for a longer slit. This results in a dark area in the upper and lower part of the captured spectrograms. The frames shown in this chapter are therefore cropped. Images from the HSI V4 show pixel 220 to 780 on the y-axis, while for the images from the HSI V6 the pixel range 405 to 1280 was used.

## 4.1 Spectral Calibration

The results of the spectral calibration are the coefficients from the polynomial fit, as mentioned in Section 3.2. For simplicity, and to avoid the smile effect as the spectral calibration was done separately from the smile and keystone corrections, only the middle line in each image was used to calculate the coefficients. Coefficients for several images were then calculated, and the average values used as the final coefficients. The spectral calibration coefficients found for the HSI V4 and the HSI V6, together with the calculated spectral range, can be seen in Table 4.1.

*Table 4.1: Spectral calibration results for both imagers, the polynomial fit coefficients, given as the mean values  $\pm$  standard deviation.*

| Imager | Polynomial fit coefficients  | Spectral range    |
|--------|--|-------------------|
| HSI V4 | $a_0 = 299.3 \pm 2.03$<br>$a_1 = 0.3295 \pm 6.55 \cdot 10^{-3}$<br>$a_2 = 9.7217 \cdot 10^{-6} \pm 4.82 \cdot 10^{-6}$ | 299.3 - 1015.0 nm |
| HSI V6 | $a_0 = 377.8 \pm 0.019$<br>$a_1 = 0.2300 \pm 8.46 \cdot 10^{-5}$<br>$a_2 = 3.778 \cdot 10^{-7} \pm 4.98 \cdot 10^{-8}$ | 377.8 - 851.2 nm  |

As spectral calibration maps from spectral pixel to wavelength, the result when applied to the spectrogram is a change in the spectral axis. The axis after spectral calibration can be seen in Figure 4.7, together with the peaks observed and used for spectral calibration of the HSI V4. The spectral calibration coefficients are applied using Equation 3.1.

The imager specifications in Table 3.1 shows an expected spectral range of 297.5 to 1005.5 nm for the HSI V4, and 400 to 800 nm for the HSI V6. The results from the spectral calibration indicates a spectral range of about 300 to 1015 nm for the HSI V4, which is quite close to the specified range. For the HSI V6, the spectral range is a bit greater than the specification, reaching wavelengths exceeding both the lower and upper range. The calculated spectral range covers the full spectral axis. The true spectral range are shorter, however, as it is limited by an anti-reflection coating that blocks light below 400 nm and by second order effects that may appear above 800 nm, for both imagers.

## 4.2 Radiometric Calibration

The radiometric calibration was performed on both the HSI V4 and the HSI V6, as described in Section 3.3. First, the average dark current in the imagers was estimated, then the radiometric coefficients were calculated. A more thorough analysis of both the dark current and the radiometric sensor response as a function of exposure time is presented in 4.3.3.

### 4.2.1 Dark Current

For the dark current analysis, a small number of counts varying for each pixel was expected. The count could also vary for each pixel between different exposures. The average dark current value for both imagers are shown in Table 4.2. The average value is found by first finding the average dark current in every pixel in the whole frame, and then average of this value for about 30 frames for each imager. It can be seen that both imagers has an estimated dark current of about 7-8 counts. While the HSI V4 has a slightly lower count, it has also greater variance in the measurements.

*Table 4.2: Estimated values for dark current, given as mean  $\pm$  standard deviation.*

| HSI | Settings                     | Average counts                  |
|-----|------------------------------|---------------------------------|
| V4  | fps = 20, gain = 0, exp = 20 | $7.289 \pm 0.7630$              |
| V6  | fps = 5, gain = 0, exp = 10  | $8.368 \pm 4.389 \cdot 10^{-3}$ |

An example of dark current count values in the middle line of the spectrogram can be seen in Figure 4.1 and Figure 4.2, for the HSI V4 and HSI V6, respectively. It can be seen that the dark current values greatly varies in the HSI V4, while the counts in the HSI V6 is centred around the average count. An example of the distribution of dark current counts in the whole spectrogram can be seen in Figure 4.3 for the HSI V4 and in Figure 4.4 for the HSI V6. By comparing these images, it can be seen that the dark current is more uniform in the HSI V6, while traces of patterns are apparent for the HSI V4.

An average frame, holding the average dark current count for each pixel, can be seen in Figure 4.5 and Figure 4.6, for the HSI V4 and HSI V6, respectively. The average dark current values are clearly more uniform for the HSI V6. Using a single dark current value as the dark current estimate in the radiometric calibration should therefore be no problem for the HSI V6. For the HSI V4, however, it can be seen that the middle spectral pixels in general hold higher dark current counts, while the higher spectral pixels hold quite low values. Using a

single value estimate for this case will not be as accurate, and a full matrix holding a dark current estimate for each individual pixel should be considered. This was not discovered until after the radiometric calibration of the HSI V6, however. The HSI V4, calibrated using the same procedure, was therefore calibrated using a single dark current value estimate as well. This should be improved in future calculations.

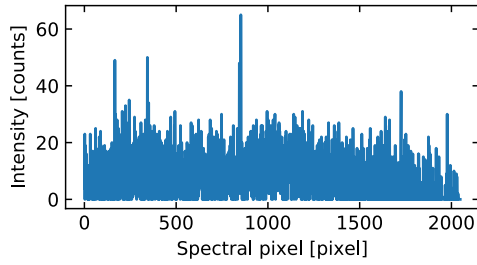


Figure 4.1: Example of dark current values and distribution in the middle horizontal line of the spectrogram, HSI V4.

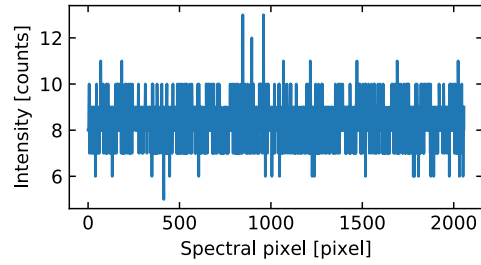


Figure 4.2: Example of dark current values and distribution in the middle horizontal line of the spectrogram, HSI V6.

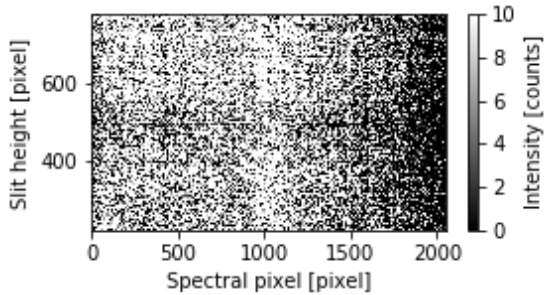


Figure 4.3: Example of dark current values and distribution within a frame, HSI V4.

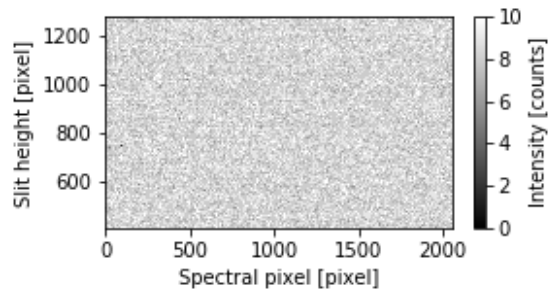


Figure 4.4: Example of dark current values and distribution within a frame, HSI V6.

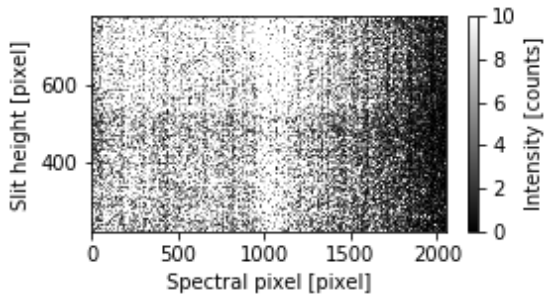


Figure 4.5: Average dark current values and distribution within a frame, HSI V4.

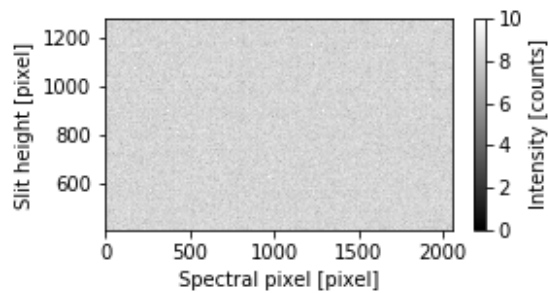


Figure 4.6: Average dark current values and distribution within a frame, HSI V6.

### 4.2.2 Radiometric

The result of the radiometric calibration of the imagers is the calibration coefficient matrix,  $\mathbf{K}_s$ , calculated using Equation 3.2.  $\mathbf{K}_s$  is the same size as the belonging spectrogram, containing a calibration coefficient for each pixel in the frame, and can therefore be applied on the whole frame using

$$\mathbf{L} = \mathbf{K}_s \cdot \mathbf{C}_{\text{per s}} \left[ \frac{\text{mW}}{\text{m}^2 \text{ sr nm}} \right], \quad (4.1)$$

to obtain a calibrated spectrogram with values in radiance instead of background corrected sensor counts per second.

Figure 4.7 shows the argon and mercury-argon peaks used for spectral calibration, the measured radiance from radiometric calibration, and the reference spectrum from the tungsten halogen lamp in the integrating sphere. The observed data is measured in counts, while the reference data is used to convert from counts to spectral radiance.

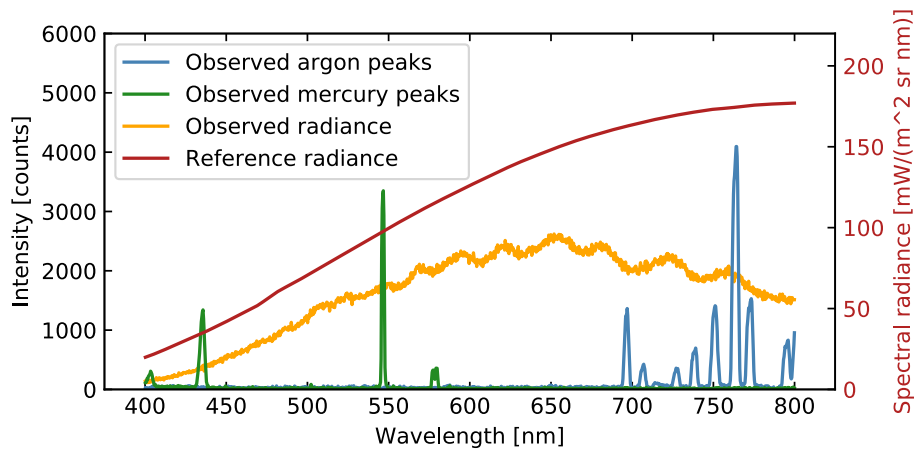


Figure 4.7: The observed argon and mercury-argon peaks from spectral calibration, the observed signal from the radiometric calibration (left), and the reference spectrum of the tungsten halogen lamp in the integrating sphere (right).

An example of spectrograms before calibration can be seen in Figure 4.8 and Figure 4.9 for the HSI V4 and HSI V6, respectively. The settings used are the same as the ones used for the dark current data in Table 4.2.

Both imagers were designed to operate in 400 to 800 nm, as the spectral range is limited by an anti-reflection coating that blocks light below 400 nm and by second order effects

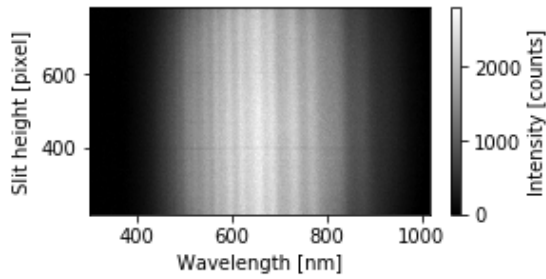


Figure 4.8: Spectrogram captured by the HSI V4 showing the integrating sphere source before calibration.

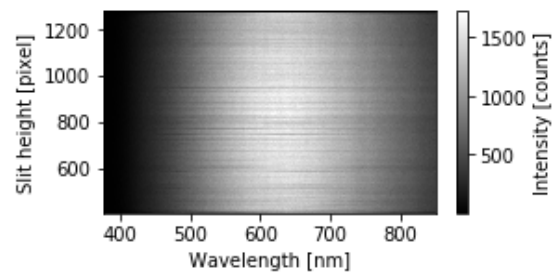


Figure 4.9: Spectrogram captured by the HSI V6 showing the integrating sphere source before calibration.

that may appear above 800 nm. The effect of the anti-reflection coating can clearly be seen in the images, as there is little to no signal below 400 nm. When looking at the higher wavelengths in Figure 4.8, the signal drops around 900 nm. This can be explained by the quantum efficiency of the sensor, as seen in Figure 4.10, as the quantum efficiency is close to 0% for the higher wavelengths. Figure 4.8 also shows some ripples, with some wavelengths being clearly brighter while others are darker for the full slit height. This pattern can also be recognised by looking at the quantum efficiency in Figure 4.10. A horizontal stripe, most likely caused by dust on the slit, can be seen at around pixel 400 in the slit height direction in Figure 4.8. Several dust stripes can also be seen for the HSI V6 in Figure 4.9. Both the ripples and the dust stripes are removed by applying the radiometric calibration coefficients.

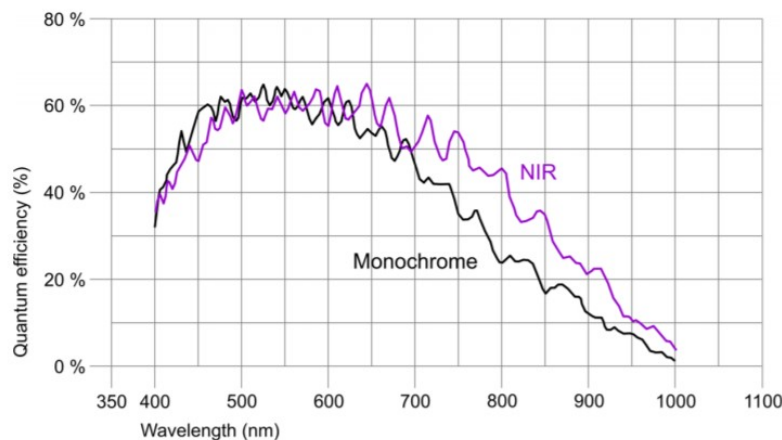


Figure 4.10: Quantum efficiency as a function of wavelength for the uEye UI-3360CP-NIR-GL camera head that is used for the HSI V4. Figure from [47].

## 4.3 Characterisation

The results from smile and keystone detection and correction are presented in Section 4.3.1, the calculated spectral bandpass in Section 4.3.2, and the result from investigation of dark current and radiometric response varying with exposure time in Section 4.3.3. All results presented in this section are calculated using data from the HSI V4.

### 4.3.1 Smile and Keystone

An example of a frame captured during data collection for smile and keystone detection can be seen in Figure 4.11. The image shows the spectral peaks from the argon spectral lamp, intersected by dark stripes created by the striped pattern in front of the collimator lens. As the wavelengths of the spectral peaks are known, and the size and distances between the spatial stripes are known, the true position of the intersection points created could be found. The position of the detected intersection points, which were used as the GCPs, were then compared to the known reference position of each point, to make a distortion model. The correction was then made by using Equation 2.19, with the calculated model coefficients  $\hat{A}$  and  $\hat{B}$ , as described in Section 2.4.2.

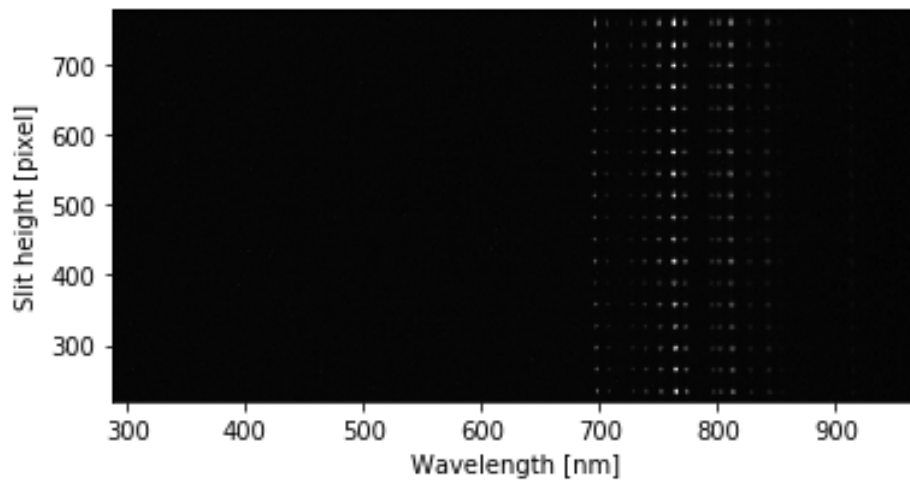


Figure 4.11: GCPs created by the striped pattern in combination with argon spectral lamp.

To obtain an even sharper pattern than seen in Figure 4.11, the aperture of the collimator lens should be adjusted to be as small as possible while still letting through enough light to illuminate the full FOV of the imager. This was discovered after the data was collected, and maximum aperture on the collimator lens was therefore used for this data instead.

A horizontal line in the frame is shown in Figure 4.12, and shows the position and strength of the argon spectral peaks used. A vertical line, within a spectral peak, can be seen in Figure 4.13 to show the positions of the striped pattern along the full slit height.

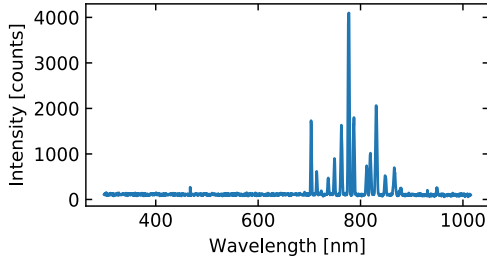


Figure 4.12: Horizontal line in the spectrogram, showing the spectral peaks.

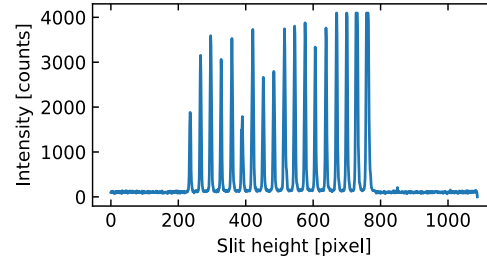
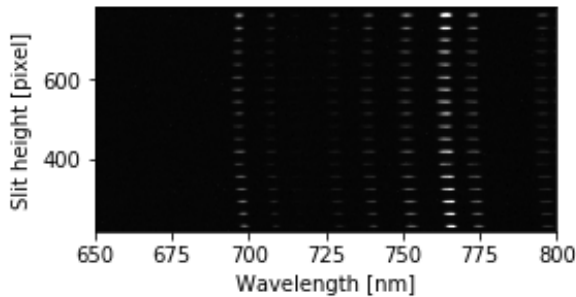
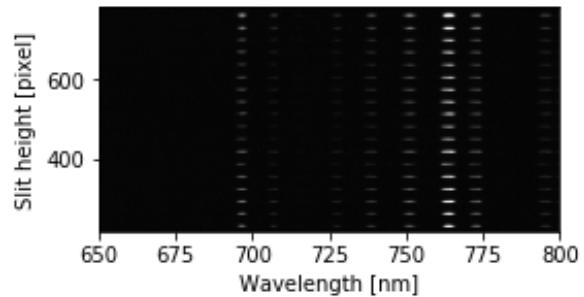


Figure 4.13: Vertical line in the spectrogram, showing the spatial stripes.

A chosen area of the frame is shown to better view the argon lines used. The curvature of the spectral lines are visible before correction in Figure 4.14a, indicating a high smile effect, while the keystone effect does not appear as extreme. The same frame after correction can be seen in Figure 4.14b, where the lines now appear straight, indicating less smile effect in the image after correction.



(a) Before correction.



(b) After correction.

Figure 4.14: Before and after smile and keystone correction.

The reduction of smile and keystone in the HSI V4 can be seen in Figure 4.15 and Figure 4.16. Figure 4.15 shows the average and maximum smile effect before and after correction for the cropped slit height. The correction shows clear improvement, and the average smile after correction is close to zero.

Figure 4.16 shows the maximum shift due to keystone before and after correction, and shows again improvement. The error after correction does not centre around zero, however. This

could be because the GCPs used all are in the right side of the image, giving a poorer estimate for the keystone effect than if the GCPs were spread evenly along the spectral axis. Combining GCPs from the argon lamp with data collected using the mercury-argon lamp could give a better estimation of the keystone effect. This should be done in future corrections.

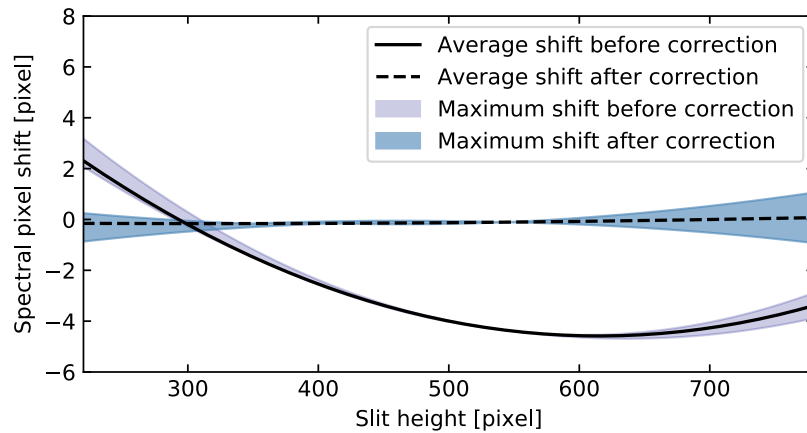


Figure 4.15: Reduction of errors due to smile.

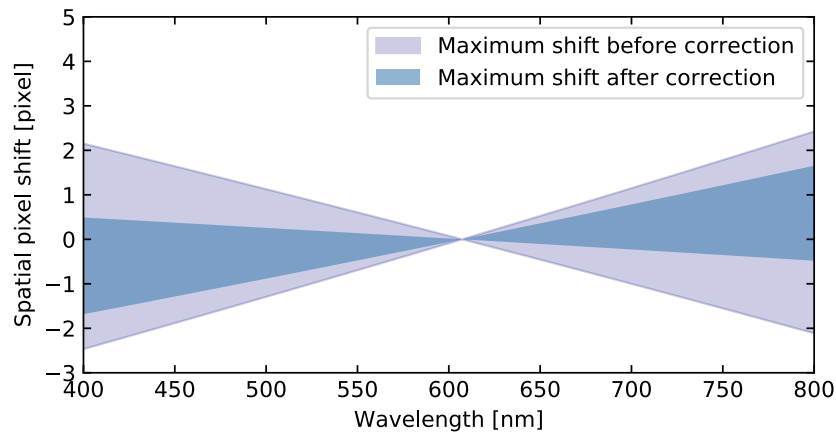


Figure 4.16: Reduction of errors due to keystone.

### 4.3.2 Spectral Bandpass

The spectral bandpass found for the HSI V4 and HSI V6 can be seen in Table 4.3. An example of the FWHM detected for a frame showing both argon and mercury-argon peaks captured with the HSI V4 can be seen in Figure 4.17.

Table 4.3: The estimated spectral bandpass for HSI V4 and HSI V6. The spectral bandpass is given as the average value  $\pm$  standard deviation.

| Imager | Avg FWHM [nm]   | FWHM at 547 nm [nm] |
|--------|-----------------|---------------------|
| HSI V4 | $4.21 \pm 0.63$ | $2.66 \pm 0.075$    |
| HSI V6 | $4.26 \pm 1.12$ | $2.84 \pm 0.0067$   |

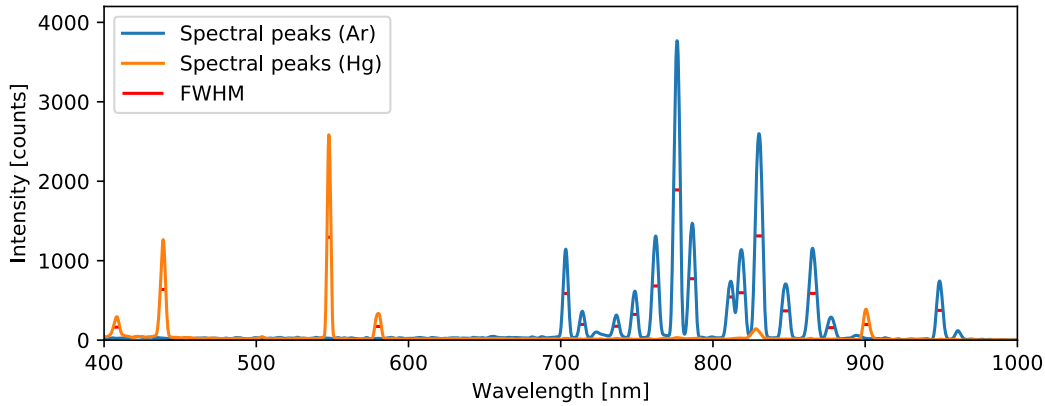


Figure 4.17: Example of spectral bandpass found in argon peaks for the HSI V4.

The theoretical FWHM for the HSI V4 and HSI V6, found in Table 3.1, are 1.4 nm and 3.3 nm, respectively. The estimated average bandpass for both imagers are worse than the given values. When taking the standard deviation into account the bandpass for HSI V6 comes close to the specified value, while the one estimated for HSI V4 is still off. When looking at the bandpass of the mercury peak at 547 nm, close to the designed centre wavelength at 553 nm, however, the spectral bandpass gets lower for both imagers. The values are still not as good as the specified bandpass for the HSI V4, but the HSI V6 shows better performance at this peak than the specified spectral bandpass for the imager.

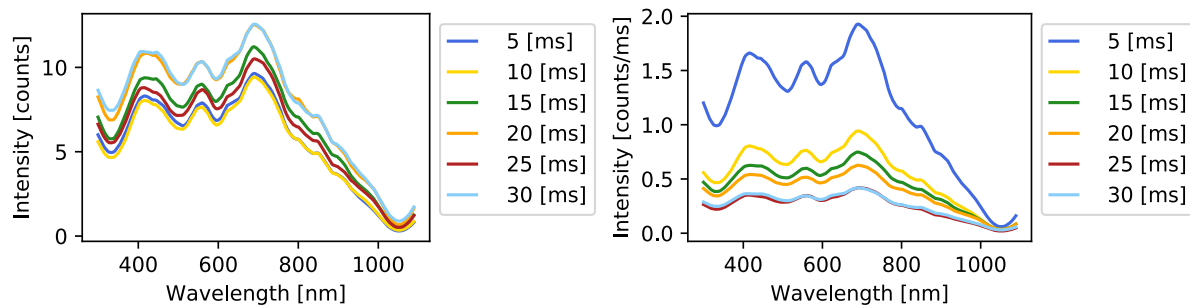
As seen in Figure 4.17, the width found for the double peaks are not the ones at half maximum. The better choice would be to remove the estimate from these peaks, as the full width at half maximum is not visible in these cases. Peaks from more spectral lamps, such as the xenon and krypton lamps, should also be included in the estimation. In some cases, it looks like the peaks are more narrow for lower wavelengths, which may be true as the optical design is optimised with centre wavelength 553 nm. It is therefore expected that the peaks closer to this wavelengths are more narrow than the ones further away.

### 4.3.3 Sensor Response

To better observe trends in the data as a function of exposure time, only the response in the middle line of the spectrograms were analysed, as looking at the full frame would be to include too much information at once. The response was also smoothed a lot, with a window of about 200 pixels, to filter out as much noise as possible. An example of an unfiltered line with dark current measurements can be seen in Figure 4.1, in Section 4.2.1. Comparing the response without filtering gave no clear indication of the changes in average response with exposure time. As this analysis was done to investigate these trends, the heavy filtering was therefore deemed necessary.

#### Dark Current

As seen in Figure 4.18a, the dark current count in the middle line increases slightly as the exposure time increases. In Figure 4.18b, however, which shows the response per millisecond, it becomes clear that the dark current count per millisecond is not constant. Estimating the dark current value per exposure time is therefore not necessarily a good solution.



(a) Total dark current count.

(b) Dark current count per millisecond.

Figure 4.18: Smoothed average dark current response in the middle horizontal line of spectrograms captured by the HSI V4 at different exposure times.

Figure 4.19 shows the average dark current count (single value) in the average middle line of the spectrograms. A linear fit was made to show the slight increase in average counts with exposure time. When looking at the standard deviation, however, it becomes clear that using a single dark current value estimate for the radiometric calibration of the HSI V4 gives greater uncertainties than the variation in dark current counts with exposure time. If a full

matrix with the estimated dark current values for every pixel in the frame is implemented for the radiometric calibration, further investigation of the dark current variations with exposure time should be included.

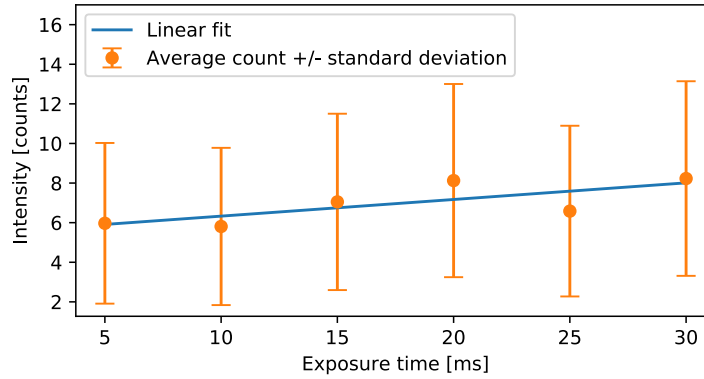
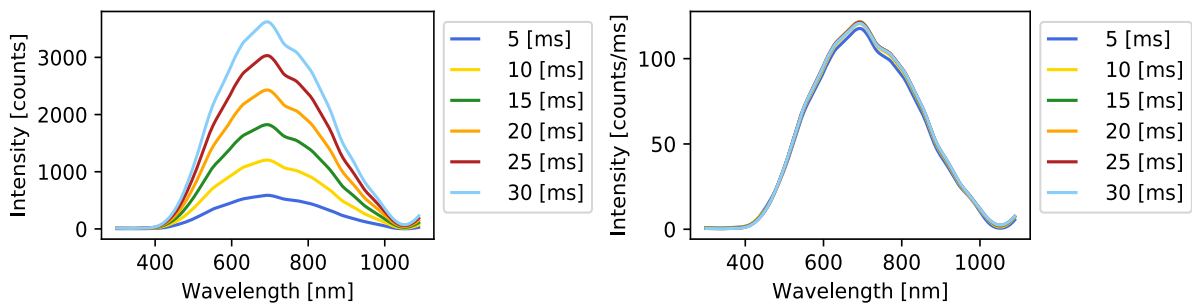


Figure 4.19: Average dark current value in each middle line plus/minus the standard deviation, shown together with a linear fit of the dark current value per exposure time.

### Radiometric

The average radiometric response in the middle line of the spectrograms captured at different exposure times are shown in Figure 4.20a, and shows a clear dependence of measured counts varying with exposure time. Figure 4.20b shows the average radiometric response per millisecond. It can be seen that the response per millisecond is approximately equal for all data sets, suggesting a close to linear sensor response.



(a) Total radiometric response.

(b) Radiometric response per millisecond.

Figure 4.20: Smoothed average radiometric response in the middle horizontal line of spectrograms captured by the HSI V4 at different exposure times.

## 5 | Conclusion and Further Work

The aim of this project was to set up spectral and radiometric calibration procedures, and implement a method for automatic detection and correction of smile and keystone effects in hyperspectral imagers.

Spectral and radiometric calibration procedures were set up, and data collected for two hyperspectral imagers, the HSI V4 and the HSI V6. The calibration coefficients were calculated, and both spectral and radiometric calibration performed. Testing and verification of the calibration performance is yet to be investigated. The spectral ranges calculated from the spectral calibration coefficients were within the expected ranges for both imagers. In radiometric calibration, it was found that the dark current in the HSI V6 was uniform and with an average value of about 8 counts in each pixel. The dark current in the HSI V4, however, had stronger variations, and was not evenly distributed. Using a single value estimate for the dark current in radiometric calibration, as done in this project, for the HSI V4 is therefore not desirable, and a full dark current matrix should be estimated and used in future calibration of this imager.

The data from spectral calibration was further used to estimate the spectral bandpass of the imagers, which was within the expectations for the HSI V6, but not as good for the HSI V4. A larger dataset, containing the dark current and radiometric response for different exposure times, was collected for radiometric calibration of the HSI V4, and further used to investigate the linearity of the sensor response. The dark current was found to some degree with exposure time, but not linearly. But as long as a single value estimate is used for the dark current estimate, the single value estimate itself introduces far greater error than the variation of the dark current with exposure time. The radiometric response, on the other hand, was found to have a close to linear variation with exposure time.

A set-up to detect smile and keystone in the imagers was designed and built, and a method to make corrections for these effects implemented. The results show that both smile and keystone was reduced after correction, but improvements can still be made, especially for keystone. The detection algorithm should be further developed to include data from several spectral lamps to improve the keystone detection, and by this improve the distortion model which again will improve the corrections.

In addition, a characterisation set-up to detect changes in the radiometric response due to radiation effects was built and tested. The set-up was then used during radiation testing at the Technical University of Denmark (DTU) in the spring of 2019. The characterisation set-up consisted of an optical table with a stable light source, white paper used as a diffuser, and a mount for the imager. The paper was illuminated by the light source, and the imager pointed towards the paper. This was used to measure the radiometric response between each radiation dose. Analysis was then done to investigate the effects of radiation on the sensor and lenses. A more detailed description of the experiment can be found in [48].

As a part of future work for this project, the data from radiometric calibration can further be used to find the SNR, and the dynamic range of the imagers. A set-up for detecting the PSF should be developed for a more thorough characterisation of the system, as done in [29]. Other effects, such as temperature dependency, stray light, and polarisation sensitivity, as mentioned in [13], should also be characterised. In addition, since the hyperspectral imagers used in this report will be used in remote sensing, procedures and methods for performing calibration and corrections in-flight and in-orbit should be investigated and developed.

# Bibliography

- [1] M. B. Henriksen, *Hyperspectral Imager Calibration and Characterisation*. Specialisation project, Norwegian University of Science and Technology, 2018.
- [2] M. T. Eismann, *Hyperspectral Remote Sensing*. SPIE, 2012.
- [3] K. Lenhard, *Improving the Calibration of Airborne Hyperspectral Sensors for Earth Observation*. PhD thesis, University of Zürich, 2015.
- [4] P. M. Gilbert, D. M. Anderson, P. Gentien, E. Granéli, and K. G. Sellner, “The Global Complex Phenomena of Harmful Algal Blooms,” *Oceanography*, vol. 18, no. 2, pp. 136–147, 2005.
- [5] G. Johnsen, R. Dalløkken, W. Eikrem, C. Legrand, J. Aure, and H. R. Skjoldal, “Eco-physiology, bio-optics and toxicity of the ichthyotoxic *Chrysochromulina leadbeateri* (Prymnesiophyceae),” *Journal of Phycology*, vol. 35, pp. 1465–1476, 1999.
- [6] G. Johnsen, Z. Volent, K. Tangen, and E. Sakshaug, “Time series of harmful and benign phytoplankton blooms in northwest European waters using the Seawatch buoy system,” in *Monitoring Algal Blooms: New Technologies for Detecting Large-Scale Environmental Change.*, ch. 6, pp. 113–141, Springer - Verlag and Landes Bioscience, 1997.
- [7] J. H. Landsberg, “The Effects of Harmful Algal Blooms on Aquatic Organisms,” Tech. Rep. 2, 2002.
- [8] M. E. Grøtte *et al.*, “Hyperspectral Imaging Small Satellite in Multi-Agent Marine Observation System,” 2018. unpublished.
- [9] K. Rajan, T. A. Johansen, and R. Birkeland, “A Roadmap for a SmallSat Program,” 2016. unpublished.
- [10] J. S. Pearlman, P. S. Barry, C. C. Segal, J. Shepanski, D. Beiso, and S. L. Carman, “Hyperion, a space-based imaging spectrometer,” *IEEE Transactions on Geoscience and Remote Sensing*, vol. 41, no. 6, pp. 1160–1173, 2003.
- [11] R. L. Lucke *et al.*, “The hyperspectral imager for the coastal ocean (hico) - design and early results,” *IGRSS Workshop on Hyperspectral Image and Signal Processing: Evolution in Remote Sensing*, pp. 1–4, 2010.
- [12] J. Transon, R. D’Andrimont, A. Maignard, and P. Defourny, “Survey of Hyperspectral Earth Observation Applications from Space in the Sentinel-2 Context,” *Remote Sensing*, vol. 10, no. 157, pp. 1–32, 2018.
- [13] C. McClain and G. Meister, *Mission Requirements for Future Ocean-Colour Sensors*, vol. 13. IOCCG, 2012.
- [14] P. Gege, J. Fries, P. Haschberger, P. Schötz, H. Schwarzer, P. Strobl, B. Suhr, G. Ulbrich, and W. Jan Vreeling, “Calibration Facility for Airborne Imaging Spectrometers,” *ISPRS Journal of Photogrammetry and Remote Sensing*, vol. 64, pp. 387–397, 2009.
- [15] X. Yu, Y. Sun, A. Fang, W. Qi, and C. Liu, “Laboratory Spectral Calibration and Radiometric Calibration of Hyper-spectral Imaging Spectrometer,” in *ICSAI: 2nd International Conference on Systems and Informatics, ICSAI 2014*, pp. 871–875, 2015.
- [16] F. Sigernes, “Basic Hyper Spectral Imaging,” 2018. Lecture notes NTNU, Retrieved from [http://kho.unis.no/doc/TTK20/BASIC\\_HYPER\\_SPECTRAL\\_IMAGING.pdf](http://kho.unis.no/doc/TTK20/BASIC_HYPER_SPECTRAL_IMAGING.pdf).
- [17] G. Joseph, *Building Earth Observation Cameras*. Taylor & Francis Group, 2015.
- [18] Y. Zong, S. W. Brown, G. Meister, R. A. Barnes, and K. R. Lykke, “Characterization and Correction of Stray Light in Optical Instruments,” *Proc. of SPIE: Sensors, Systems, And Next-Generation Satellites XI*, vol. 6744, 2007.

- [19] T. Skauli, H. E. Torkildsen, S. Nicolas, T. Opsahl, T. Haavardsholm, I. Kåsen, and A. Rognmo, "Compact Camera for Multispectral and Conventional Imaging Based on Patterned Filters," *Applied Optics*, vol. 53, no. 13, pp. C64–C71, 2014.
- [20] R. A. Schowengerdt, "Chapter 9: Thematic Classification," in *Remote Sensing - Models and Methods for Image Processing*, 2007.
- [21] P. Mouroulis and M. M. McKerns, "Pushbroom imaging spectrometer with high spectroscopic data fidelity: experimental demonstration," *Optical Engineering*, vol. 39, no. 3, pp. 808–816, 2000.
- [22] G. Yang, C. Li, Y. Wang, H. Yuan, H. Feng, B. Xu, and X. Yang, "The DOM Generation and Precise Radiometric Calibration of a UAV-Mounted Miniature Snapshot Hyperspectral Imager," *Remote Sensing*, vol. 9, no. 642, pp. 1–21, 2017.
- [23] P. Mouroulis, R. O. Green, and T. G. Chrien, "Design of Pushbroom Imaging Spectrometers for Optimum Recovery of Spectroscopic and Spatial Information," *Applied Optics*, vol. 39, no. 13, pp. 2210–2220, 2000.
- [24] F. Sigernes, J. M. Holmes, M. Dyrland, D. A. Lorentzen, S. A. Chernous, T. Svinyu, J. Moen, and C. S. Deehr, "Absolute calibration of optical devices with a small field of view," *J. Opt. Technol.*, vol. 74, no. 10, pp. 669–674, 2007.
- [25] T. Skauli, "Feasibility of a Standard for Full Specification of Spectral Imager Performance," *Proc. of SPIE: Hyperspectral Imaging Sensors: Innovative Applications and Sensor Standards*, vol. 10213, pp. 1–12, 2017.
- [26] D. Tao, G. Jia, Y. Yuan, and H. Zhao, "A Digital Sensor Simulator of the Pushbroom Offner Hyperspectral Imaging Spectrometer," *Sensors (Switzerland)*, vol. 14, pp. 23822–23842, 2014.
- [27] P. Mouroulis, D. A. Thomas, T. G. Chrien, V. Duval, R. O. Green, J. J. Simmonds, and A. H. Vaughan, "Trade Studies in Multi/hyperspectral Imaging Systems Final Report," tech. rep., Jet Propulsion Laboratory, 1998.
- [28] N. Yokoya, N. Miyamura, and A. Iwasaki, "Preprocessing of hyperspectral imagery with consideration of smile and keystone properties," in *Proc. SPIE 7857, Multispectral, Hyperspectral, and Ultraspectral Remote Sensing Technology, Techniques, and Applications III*, vol. 78570B, 2010.
- [29] T. Skauli and H. E. Torkildsen, "Measurement of Point Spread Function for Characterization of Coregistration and Resolution: Comparison of Two Commercial Hyperspectral Cameras," *Proc. of SPIE: Algorithms and Technologies for Multispectral, Hyperspectral, and Ultraspectral Imagery XXIV*, vol. 10644, no. May, 2018.
- [30] T. Skauli, "An Upper-Bound Metric for Characterizing Spectral and Spatial Coregistration Errors in Spectral Imaging," *Optics Express*, vol. 20, no. 2, pp. 918–933, 2012.
- [31] A. Fridman, G. Høye, and T. Løke, "Resampling in Hyperspectral Cameras as an Alternative to Correcting Keystone in Hardware, with Focus on Benefits for Optical Design and Data Quality," *Optical Engineering*, vol. 53, no. 5, 2014.
- [32] K. C. Lawrence, B. Park, W. R. Windham, and C. Mao, "Calibration of a Pushbroom Hyperspectral Imaging System for Agricultural Inspection," *Transaction of the ASAE*, vol. 46, no. 2, pp. 513–521, 2003.
- [33] H. E. Torkildsen and T. Skauli, "Full Characterization of Spatial Coregistration Errors and Spatial Resolution in Spectral Imagers," *Optics Letters*, vol. 43, no. 16, pp. 3814–3817, 2018.
- [34] N. Yokoya, N. Miyamura, and A. Iwasaki, "Detection and Correction of Spectral and Spatial Misregistrations for Hyperspectral Data using Phase Correlation Method," *Applied Optics*, vol. 49, no. 24, pp. 4568–4575, 2010.
- [35] D. Z. für Luft-und Raumfahrt e.V., "The calibration home base for imaging spectrometers," *Journal of large-scale research facilities*, vol. 2, no. A82, 2016.
- [36] Y. Feng and Y. Xiang, "Mitigation of spectral mis-registration effects in imaging spectrometers via cubic spline interpolation," *Optics Express*, vol. 16, no. 20, pp. 15366–15374, 2008.

- [37] R. O. Green, "Spectral calibration requirement for Earth-looking imaging spectrometers in the solar-reflected spectrum," *Applied Optics*, vol. 37, no. 4, pp. 683–690, 1998.
- [38] H. R. Gordon, T. Du, and T. Zhang, "Atmospheric correction of ocean color sensors: analysis of the effects of residual instrument polarization sensitivity," *Applied Optics*, vol. 36, no. 27, pp. 6938–6948, 1997.
- [39] G. Meister, E. J. Kwiatkowska, B. A. Franz, F. S. Patt, G. C. Feldman, and C. R. McClain, "Moderate-Resolution Imaging Spectroradiometer ocean color polarization correction," *Applied Optics*, vol. 44, no. 26, pp. 5524–5535, 2005.
- [40] G. W. Kattawar, G. N. Plass, and J. A. Guinn, "Monte Carlo Calculations of the Polarization of Radiation in the Earth's Atmosphere-Ocean System," *Journal of Physical Oceanography*, vol. 3, no. 4, pp. 353–372, 1973.
- [41] W. Dietmar, "Image Flare measurement according to ISO 18844," *Electronic Imaging*, vol. 2016, no. 18, pp. 1–7, 2017.
- [42] ISO 9358, "Optics and optical instruments – veiling glare of image forming systems – definitions and methods of measurement," 1998.
- [43] Oriol Instruments, "Typical Spectra of Oriol Instruments Spectral Calibration Lamps." Retrieved from [https://www.newport.com/medias/sys\\_master/images/h55/hfd/8797293281310/Typical-Spectra-of-Spectral-Calib-Lamps.pdf](https://www.newport.com/medias/sys_master/images/h55/hfd/8797293281310/Typical-Spectra-of-Spectral-Calib-Lamps.pdf).
- [44] F. Sigernes, M. Syrjäsuo, R. Storvold, J. Fortuna, M. E. Grøtte, and T. A. Johansen, "Do It Yourself Hyperspectral Imager for Handheld to Airborne Operations," *Optics Express*, vol. 26, no. 5, pp. 6021–6035, 2018.
- [45] F. Sigernes *et al.*, "Pushbroom Hyper Spectral Imager version 6 (HSI v6) part list – Final prototype," 2018.
- [46] M. B. Henriksen, J. L. Garrett, E. F. Prentice, A. Stahl, T. A. Johansen, and F. Sigernes, "Real-time corrections for a low-cost hyperspectral instrument." 2019.
- [47] IDS, "UI-3360CP-NIR-GL Rev.2 (AB00624)." Retrieved from [https://en.ids-imaging.com/IDS/datasheet\\_pdf.php?sku=AB00624](https://en.ids-imaging.com/IDS/datasheet_pdf.php?sku=AB00624).
- [48] V. R. Kristvik, *The Effect of Radiation on Optical Elements for a Hyperspectral CubeSat Payload*. Bachelor's thesis, Norwegian University of Science and Technology, 2019.
- [49] Gigahertz-Optik GmbH, "Calibration certificate," 2013.



# Appendices



# A | Data Collection Procedures

This chapter describes the procedures for collecting data used in spectral and radiometric calibration, as well as the data used for smile and keystone correction. All procedures are assumed to be performed in a dark room with the equipment described in Section 3.1.

## A.1 Spectral Calibration

Collecting the data:

1. Take an image of initial lab set-up, as reference for when cleaning up later.
2. Remove the cap off the integrating sphere inlet.
3. Remove the cap off the lamp inlet using small hex keys.
4. Prepare the calibration lamp mounts. The mounts should be placed so that the lamp is held in the inlet of the integrating sphere.
5. Prepare the HSI. Connect to laptop, start capturing software and make sure the imager is running properly by taking a test image. Remove the HSI lens cover.
6. Prepare the HSI mount and attach the HSI. Make sure that the opening in the integrating sphere covers the entire FoV of the imager.
7. Attach the calibration lamp (note the type) to the mount and secure in inlet.
8. Connect lamp power supply, make sure the power switch is turned off.
9. Take a normal photo of the set-up.
10. Turn the lamp on, note the time in attached log. Check if the lamp needs any warm-up time, and wait if needed. Turn all other lights off.
11. Set correct imager parameters: AOI, frame rate, exposure time, binning, gain.
12. Take a test image, note the time to know how long the lamp warmed up before use. Check that the test image is not over- or underexposed. If it is, adjust the settings and take new test image. Repeat until the test image is no longer over- or underexposed.
13. Take a series of images, preferably more than 30. Note the time, and save the .ini file in the folder with the images. Include date, imager and lamp type in the name of the folder.
14. Turn lab lights back on.
15. Turn the calibration lamp off, and note the time in the attached log.
16. Repeat steps 7 - 15 above for all calibration lamps.
17. Turn off the imager, unplug the lamp power supply and clean up. Look at reference image to make sure the lab looks the same as before the calibration.

## A.2 Radiometric Calibration

The radiometric calibration consists of two parts; characterising the dark current, and comparing calibration data with known reference data, as described in Section 3.3. Both dark current data and radiometric data must therefore be collected.

### A.2.1 Dark Current Data

Collecting the data:

1. Take an image of initial lab set-up, as reference for when cleaning up later.
2. Prepare the HSI. Connect to laptop, start capturing software and make sure the imager is running properly by taking a test image.
3. Make sure the lens cap is on. Place the imager in a dark place, preferably a box or something similar, to shield it from any light sources such as the laptop.
4. Set correct imager parameters: AOI, frame rate, exposure time, binning, gain.
5. Turn all lights off.
6. Take a series of images, preferably more than 30. Note the time, and save the .ini file in the folder with the images. Include date, imager, exposure time and frame rate in the name of the folder.
7. Optional: Repeat step 6 for different settings/ exposure times.
8. Turn lab lights back on. Turn off the imager.
9. Continue with the radiometric calibration procedure, or clean up. If cleaning up, look at reference image to make sure the lab looks the same as before the calibration.

### A.2.2 Radiometric Data

Collecting the data:

1. Take an image of initial lab set-up, as reference for when cleaning up later.
2. Remove the cap off the integrating sphere inlet.
3. Make sure the fan, bulb and light sensor are properly connected to the integrating sphere. Connect the power unit.
4. Turn on the power unit using the switch on the back panel. The fan will start up and the power lamp on the front panel will start blinking.
5. Turn on the integrating sphere lamp by pressing the On/Off button on the front panel. The power lamp will blink rapidly while in ramp mode, and go steady when the lamp is on after approximately 30 seconds. Note the time when the lamp was turned on.
6. Let the lamp warm up for 20-30 minutes, before starting the measurements. Prepare the HSI and take test images while waiting.

7. Prepare the HSI. Connect to laptop, start capturing software and make sure the imager is running properly by taking a test image. Remove the HSI lens cover.
8. Prepare the HSI mount and attach the HSI. Make sure that the opening in the integrating sphere covers the entire FoV of the imager.
9. Take a normal photo of the set-up.
10. Set correct imager parameters: AOI, frame rate, exposure time, binning, gain.
11. Take a test image, note the time to know how long the lamp warmed up before use. Check that the test image is not over- or underexposed. If it is, adjust the settings and take new test image. Repeat until the test image is no longer over- or underexposed.
12. Take a series of images, preferably more than 30. Note the time, and save the .ini file in the folder with the images. Include date, imager, exposure time and frame rate in the name of the folder.
13. Turn lab lights back on.
14. Turn the integrating sphere lamp off, and note the time in the attached log. The power lamp will blink rapidly while in ramp mode, and slowly when the lamp is off. Wait 2-3 minutes before turning off the power unit, to let the fan cool down the bulb.
15. Turn off the imager, unplug the lamp power supply and clean up. Look at reference image to make sure the lab looks the same as before the calibration.

### A.3 Smile and Keystone Correction

#### Collecting the data:

1. Take an image of initial lab set-up, as reference for when cleaning up later.
2. Remove the cap off the integrating sphere inlet.
3. Remove the cap off the lamp inlet using small hex keys.
4. Prepare the calibration lamp mounts. The mounts should be placed so that the lamp is held in the inlet of the integrating sphere.
5. Prepare the HSI. Connect to laptop, start capturing software and make sure the imager is running properly by taking a test image. Remove the HSI lens cover.
6. Prepare the HSI mount and attach the HSI. Make sure that the opening in the integrating sphere covers the entire FoV of the imager.
7. Prepare the collimator lens. Mount the striped pattern onto the backside of the lens, and fasten with tape if necessary. Put the collimator lens in its holder and place this between the HSI and the integrating sphere. The lens should be as close to the HSI as possible. Make sure focus of the collimator lens is set to infinity, and adjust the aperture to be as small as possible while still letting through enough light to illuminate the full FOV of the imager.
8. Attach the calibration lamp (note the type) to the mount and secure in inlet.
9. Connect lamp power supply, make sure the power switch is turned off.
10. Take a normal photo of the set-up.
11. Turn the lamp on, note the time in attached log. Check if the lamp needs any warm-up time, and wait if needed. Turn all other lights off.
12. Set correct imager parameters: AOI, frame rate, exposure time, binning, gain.
13. Take a test image, note the time to know how long the lamp warmed up before use. Check that the test image is not over- or underexposed. If it is, adjust the settings and take new test image. Repeat until the test image is no longer over- or underexposed.
14. Take a series of images, preferably more than 30. Note the time, and save the .ini file in the folder with the images. Include date, imager and lamp type in the name of the folder.
15. Turn lab lights back on.
16. Turn the calibration lamp off, and note the time in the attached log.
17. Repeat steps 7 - 15 above for all calibration lamps.
18. Turn off the imager, unplug the lamp power supply and clean up. Look at reference image to make sure the lab looks the same as before the calibration.

## B | Lamp Certificate, ISS-30-VA

The calibration lamp certificate belonging to the integrating sphere (ISS-30-VA) used in the calibrations can be seen in Figure B.1 to B.4.

Kalibrierlaboratorium für optische Strahlungsmessgrößen  
*Calibration laboratory for optical radiometry*



## GIGAHERTZ OPTIK GMBH

**Werkskalibrierschein**  
**Calibration Certificate**

Kalibrierzeichen  
*Calibration mark*

|         |
|---------|
| 19615   |
| WERK    |
| 2013-02 |

Gegenstand  
*Object* **Homogene Lichtquelle für spektrale Strahl-dichte**  
**Homogeneous light source for spectral radiance**

Hersteller  
*Manufacturer* **Gigahertz-Optik, GmbH**

Typ  
*Type* **UMBB-300 / LPS-100-RM / X1-RM / LS-OK-30-VA / VL-1101-4**

Fabrikate/Serien-Nr.  
*Serial number* **19615aw / 13364M / 12668M / 23031**

Auftraggeber  
*Customer* **Norsk Elektro Optikk A/S**  
**Solheimveien 62A**  
**N-1473 Lorenskog NORWAY**

Auftragsnummer  
*Order No.* **PO 1012241 / (19615)**

Anzahl der Seiten des Kalibrierscheines  
*Number of pages of the certificate* **5**

Datum der Kalibrierung  
*Date of calibration* **15. February 2013**

Dieser Kalibrierschein dokumentiert die Rückführung auf nationale Normale zur Darstellung der Einheiten in Übereinstimmung mit dem Internationalen Einheitensystem (SI).

Das Kalibrierlaboratorium arbeitet in Anlehnung an die DIN EN ISO/IEC 17025. Die internen Transfernormale werden regelmäßig gegen Normale kalibriert, welche einen DKD-Kalibrierschein haben oder rückführbar auf ein Normal mit DKD-Kalibrierschein kalibriert sind oder gegen Normale eines nationalen Metrologieinstituts kalibriert sind.

Für die Einhaltung einer angemessenen Frist zur Wiederholung der Kalibrierung ist der Benutzer verantwortlich.

*This calibration certificate documents the traceability to national standards, which realise the units of measurement according to the International System of Units (SI).*

*The calibration laboratory works based to the DIN EN ISO/IEC 17025. The intern used transfer standards were regular calibrated against standards, which have DKD certificates or are traceable to a standard with DKD or National Metrology Institute certificate.*

*The user is obliged to have the object recalibrated at appropriate intervals.*

Dieser Kalibrierschein darf nur vollständig und unverändert weiterverbreitet werden. Auszüge oder Änderungen bedürfen der Genehmigung des ausstellenden Kalibrierlaboratoriums. Kalibrierscheine ohne Unterschrift und Stempel haben keine Gültigkeit.

*This calibration certificate may not be reproduced other than in full except with the permission the issuing laboratory.*

*Calibration certificates without signature and seal are not valid.*



Datum  
*Date*

15. February 2013

Leiter des Kalibrierlaboratoriums  
*Head of the calibration laboratory*

Dipl.-Ing. (FH) Anton Gugg-Helminger

Mitarbeiter im Kalibrierlabor  
*Person of Charge*

Dipl.-Ing. (FH) Richard Rendle

Figure B.1: Lamp certificate, page 1 [49].



19615

WERK

2013-02

Seite 2 zum Kalibrierschein vom 15. February 2013  
 Page of calibration certificate dated

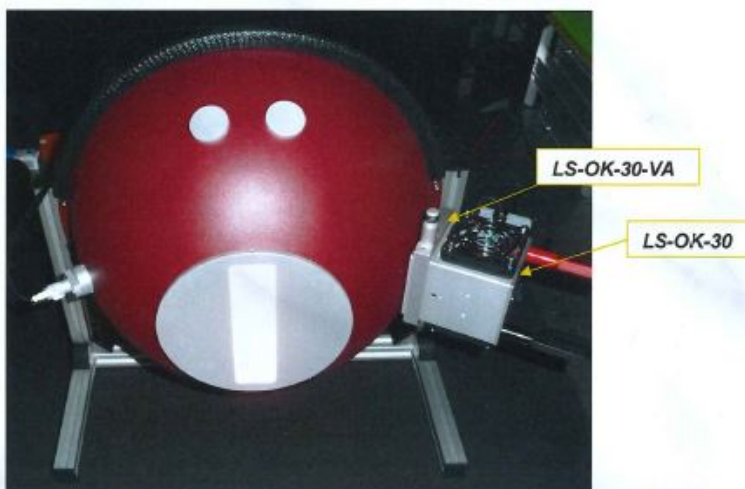
### 1. Description of the calibration object:

The calibration object is an integrating sphere, type UMBB-300 / LPS-100-RM / X1-RM / LS-OK-30-VA / VL-1101-4, SN 19615aw / 13364M / 12668M / 23031, inside made from BaSO<sub>4</sub>. The sphere is fixed inside a stable aluminium frame.

On one side of the sphere is a lamp housing with a light source, type LS-OK-30 mounted with diffuse transmitting baffle. The lamp SN L1837 is a frosted 100W QH lamp, (unfrosted type: Osram 12V, 100W, HLX 64623). On the housing frame are two cooling fan's. In front of the light source is a manually adjustable variable attenuator, LS-OK-30-VA mounted.

To connect the light source to the power supplies LPS-100-RM use the red and black cable.

On the sphere there is a photometric detector head, VL-1101-4 which is read out by the Optometer X1-RM.



Picture 1: measurement object

### 2. Measurement:

The spectral radiance was measured by using a calibration reference source, type SRS8Q, SN 7421 (Last Calibration in May 2012; GO327-WERK-2012-05), that is traceable to the PTB (Physikalisch Technischen Bundesanstalt). A monochromator (TM300) was horizontal to his input optic (telescope) measured by the calibration object and by the reference. The irradiation was measured with a silicon and a PbS detector.

### 3. Conditions during the measurement:

The calibration object and the reference were measured in rapid succession horizontal to the telescope. The measured optical surface was focused by the telescope. The measuring field of view was by  $\varnothing 7\text{mm}$ . The calibration object was calibrated by all lamps together and for the variable attenuator at 100 % intensity.

#### **Spectral bandwidth of the monochromator**

Full width half measured (FWHM)

FWHM = 10 nm for  $400\text{ nm} \leq \text{Lambda} \leq 1100\text{ nm}$

FWHM = 20 nm for  $1100\text{ nm} < \text{Lambda} \leq 2500\text{ nm}$



19615

WERK

2013-02

Seite 3 zum Kalibrierschein vom 15. February 2013  
 Page of calibration certificate dated

**Current of the lamp:**

The Reference SRS8Q, SN 7421 was operated by a dc stabilised power supply Gigahertz-Optik type LPS250, SN 3623M at a current of 4.000A.

The calibration object UM/BB-300 / LPS-100-RM / X1-RM / LS-OK-30-VA / VL-1101-4, SN 19615aw / 13364M / 12668M / 23031 was operated by using the internal power supplies LPS-100-RM of the corresponding electronic Device.

The internal current setting of the power supplies LPS-100-RM are 8.5A.

The calibration standard was set on at least 30 minutes before measurement.

**Temperature:**

Between 24 °C +/- 3 °C

**Burning time:**

2 h within the time of calibration

**4. Result of the measurement:**

Spectral radiance  $L_{e,\lambda}$  versus wavelength



Numerical value

The numerical values are on Data-CD 19615aw-k.xls

Figure B.3: Lamp certificate, page 3 [49].



19615

WERK

2013-02

Seite 4 zum Kalibrierschein vom 15. February 2013  
 Page of calibration certificate dated

| Calculated values            | 19615aw<br>UMBB-300, 100% open aperture |
|------------------------------|---|
| For lamp current             | 8.50 A                                  |
| Integrated radiance          | 42.95 W/(sr m <sup>2</sup> )            |
| Luminance                    | 7612 cd/m <sup>2</sup>                  |
| Color coordinates            | x = 0.4240<br>y = 0.4028                |
| Correlated color temperature | 3217 K                                  |
| Measuring range              | 380nm - 780nm                           |

Into the X1-RM is the following value as calibration factor stored:

|                                       |                              |
|---------------------------------------|------------------------------|
| Kalibrierfaktor<br>Calibration factor | 0.200nA/(cd/m <sup>2</sup> ) |
|---------------------------------------|------------------------------|

For the relative spectral uncertainty is following table responsible:

| Wavelength [nm]                   | Relative uncertainty [%] |
|-----------------------------------|--------------------------|
| 400nm up to 420nm in 10nm steps   | ± 6                      |
| 430nm up to 1100nm in 10nm steps  | ± 4                      |
| 1120nm up to 1500nm in 20nm steps | ± 7.5                    |
| 1520nm up to 2300nm in 20nm steps | ± 9                      |
| 2320nm up to 2350nm in 20nm steps | ± 12                     |
| 2370nm up to 2400nm in 20nm steps | ± 14                     |
| 2420nm up to 2500nm in 20nm steps | ± 15                     |

The uncertainty for the correlated colour temperature = +/- 50K.  
 The uncertainty for the luminance meter = +/- 3%.

##### 5. Remarks:

The calibration number 19615 - WERK - 2013-02 is marked on the calibration unit Type UMBB-300 / LPS-100-RM / X1-RM / LS-OK-30-VA / VL-1101-4, SN 19615aw / 13364M / 12668M / 23031. The calibration is only valid with the listed power supply. The calibration values are stored on CD.

A dependence of the spectral radiance from other as the given conditions is not examined. It is reckon in a wavelength dependence spectral radiance during the life of the lamp and a change in correlated colour temperature.

A regular recalibration of the calibrated unit type UMBB-300 / LPS-100-RM / X1-RM / LS-OK-30-VA / VL-1101-4, SN 19615aw / 13364M / 12668M / 23031 is recommended.

Figure B.4: Lamp certificate, page 4 [49].

